A reappraisal of legacy reflection seismic data from the western margin of the Kaapvaal craton, South Africa, with implications for Mesozoic-Cenozoic regional tectonics

Michael Westgate[a],*, Musa S.D. Manzi[a], Alireza Malehmir[b], Roger L. Gibson[a], Marco A.G. Andreoli[a], Adam Bumby[c]

[a]School of Geosciences, University of the Witwatersrand, P Bag 3, WITS, Johannesburg 2050, South Africa
[b]Department of Earth Sciences, Uppsala University, Villavägen 16, SE 75236, Uppsala, Sweden
[c]Department of Geology, University of Pretoria, Pretoria, South Africa

* Corresponding author:

E-mail addresses: Michael.Westgate@wits.ac.za (M. Westgate), musa.manzi@wits.ac.za (M.S.D. Manzi), alireza.malehmir@geo.uu.se (A. Malehmir), roger.gibson@wits.ac.za (R.L. Gibson), marco.andreoli@wits.ac.za (M.A.G. Andreoli), Adam.Bumby@up.ac.za (A. Bumby).

Highlights

- A legacy seismic profile on the western Kaapvaal craton border was reprocessed.
- Imaging of Phanerozoic sediments in the top 500 m was significantly improved.
- Integration of other geophysical and geological data strengthened interpretation.
- Images of Dwyka and Kalahari group structures reveal <1 Ma neotectonic activity.
- Moshaweng Fault interpreted to have undergone up to 1 Ma polyphasic reactivations.

Abstract

The 150 km long, 6 s TWT, 2D seismic profile KBF03A, which was acquired in 1994 and lies near the western edge of the Kaapvaal craton in South Africa, has been reprocessed using standard reflection seismic processing methods. The results exhibit a significant improvement in the imaging quality of the subsurface features and an evident boost in the signal-to-noise ratio. The improved seismic data, combined with application of seismic attributes, integration with surficial geological and geophysical maps, and computation of velocity tomograms, has revealed previously undetected structural features within the supracrustal sequences underlying the profile. In particular, the Phanerozoic sediments found along the profile, comprising exclusively Kalahari Group and Dwyka Group deposits, are disrupted by multiple folds of varying wavelengths (~1–10 km) and variably oriented normal and thrust faults. Additionally, the effect of the Moshaweng fault, previously characterised as a listric fault extending to depths of >10 km, on the Phanerozoic sediments has been further constrained to suggest repeated extensional reactivations and a more recent (<1 Ma) inversion. Considerations of the eastern end of the profile have suggested links between some of the observed structural features and the nearby ~146 Ma Morokweng impact structure, the lateral expanse of which is poorly constrained in the literature. The collection of these newly imaged features is interpreted as evidence for multiple Late Mesozoic to Cenozoic tectonic events, including polyphasic reactivation of basement structures, under both extensional and compressional stress regimes. By analysing these newly detected features, our study not only

provides new insight into the neotectonic evolution of the Phanerozoic sediments along the western margin of the Kaapvaal craton, but also demonstrates the utility in reprocessing legacy data and reveals its untapped potential.

Keywords: Tectonophysics; Seismotectonics; Seismology

1. Introduction

Owing to its superlative Archaean-Proterozoic mineral resources and ancient crust, South Africa has accumulated an extensive legacy geophysical database generated by mining companies and both national and international research programmes over the past 50 years. Much of the crustal (6 s TWT) seismic data acquired over the Kaapvaal craton has been focused on exploration for extensions of these mineral resources, such as the Witwatersrand Basin (Pretorius et al., 2003) and Bushveld Complex (Scheiber-Enslin and Manzi, 2018; Beukes et al., 2019). This focus on hard-rock features has meant that comparatively little attention has been devoted to investigating the internal structure of more recent, Phanerozoic, sedimentary basins that cover significant parts of the craton and, thus, its more recent tectonic history. With the significant improvement in processing algorithms and computational power in recent decades, the records of these legacy surveys provide a valuable research resource that can be further interrogated (Malajczuk et al., 2016; Manzi et al., 2018; Malehmir et al., 2019; Manzi et al., 2019). By properly retrieving, recovering and reprocessing legacy seismic data, the potential of the data to reveal second- and third-order subsurface geological features may be significantly enhanced, particularly where more sophisticated processing algorithms and seismic attributes are applied that were not available in past decades.

In this study, we present the results of a reprocessed, 150-km long, ESE-WNW-trending, legacy (6 s TWT) reflection seismic profile (KBF03A) that was shot in 1994 for the South African National Geophysical Programme by the Anglo American Corporation (now AngloGold Ashanti, Ltd) in the western part of the Kaapvaal craton (Fig. 1). This profile was interpreted previously as part of a larger study of Neoarchaean structures in the craton by Tinker et al. (2002). Apart from two small outcrops of Archaean-Palaeoproterozoic basement rocks, the profile exclusively crosses the variably lithified subhorizontal sediments of the Kalahari Group. This paper focuses on the upper (<1 s TWT) portion of the profile that intersected lithologies of the Kalahari Group and Karoo Supergroup. The primary goal of this paper, in addition to demonstrating the value of reprocessing the legacy seismic profile for enhanced structural imaging, is to address the structural features recognizable within the Phanerozoic sedimentary cover of the Dwyka and Kalahari groups and to place these within the context of the late- to post-Gondwana geodynamic evolution of southern Africa.

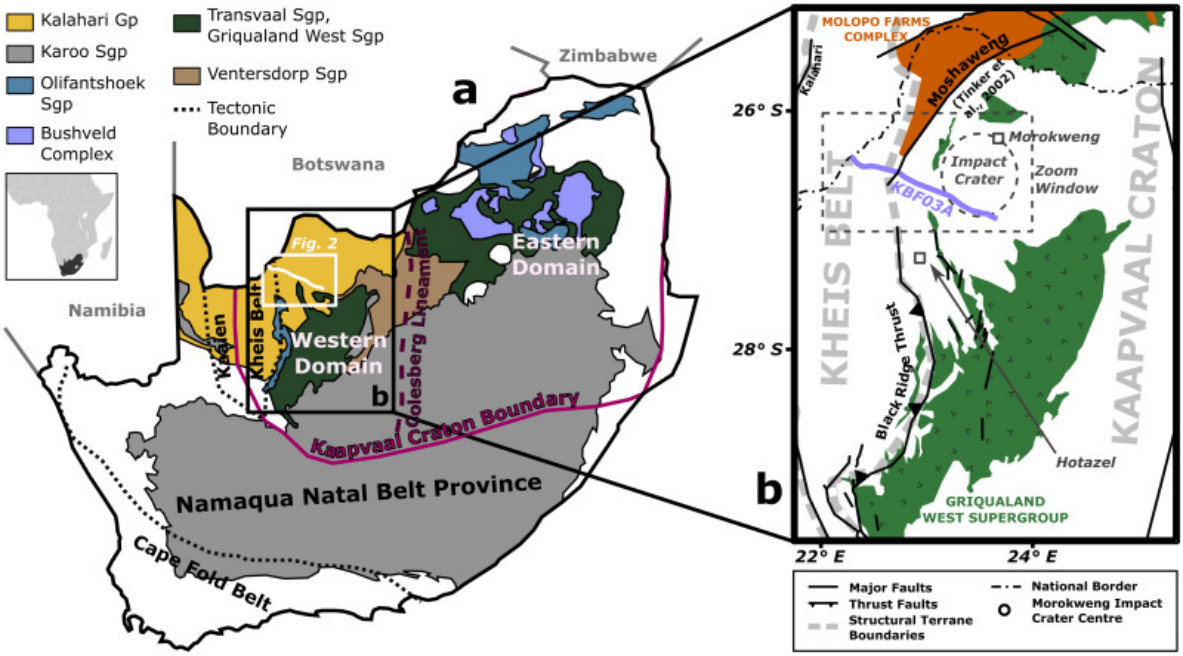

Fig. 1. Location of KBF03A profile on the Kaapvaal craton in South Africa and its position with respect to the general tectonostratigraphy of the area (a), as well as the general regional geology in the zoom window (b). Zoom b and Fig. 2 location are also highlighted in (a). Sources: Beukes et al. (2019); Tankard et al. (2012). SGp: Supergroup. Gp: Group.

2. Regional geology

The geological and geophysical context of the profile is summarised in Fig. 1, Fig. 2, Fig. 3. Much of southern Africa is covered by two major Phanerozoic sedimentary basins whose histories are closely linked to the Gondwana supercontinent cycle. The Carboniferous to Jurassic (~320–180 Ma) main Karoo Basin is interpreted as the retro-arc foreland basin formed north of the Cape orogenic belt along the southern margin of Gondwana (Catuneanu, 2004), whereas the Kalahari Basin formed as one of the world's largest (>2 million km^2) intracontinental basins following the rifting that separated Africa from South America and opened the South Atlantic at 135–115 Ma (Haddon and McCarthy, 2005; Partridge et al., 2006; Matmon et al., 2015). The eroded remnants of both basins are still present in the anomalously elevated interior plateau of southern Africa, itself the focus of research as part of the African Superswell that is attributed to as yet not fully understood mantle dynamics (e.g. Nyblade and Robinson, 1994; Lithgow-Bertelloni and Silver, 1998). Their formation accompanies that of another world-class mineral resource in southern Africa, namely, diamond-hosting kimberlite pipes, that implies a tectonically-induced lithospheric-scale plumbing system linked to asthenospheric mantle processes (e.g. Jelsma et al., 2009). However, compared to the coastal regions of southern Africa (Cape Fold Belt, Atlantic and Indian margin rift shoulders), details of the post-Carboniferous tectonic development of the interior plateau of the subcontinent – much of which is underlain by the Kaapvaal craton (Fig. 1) - are poorly understood.

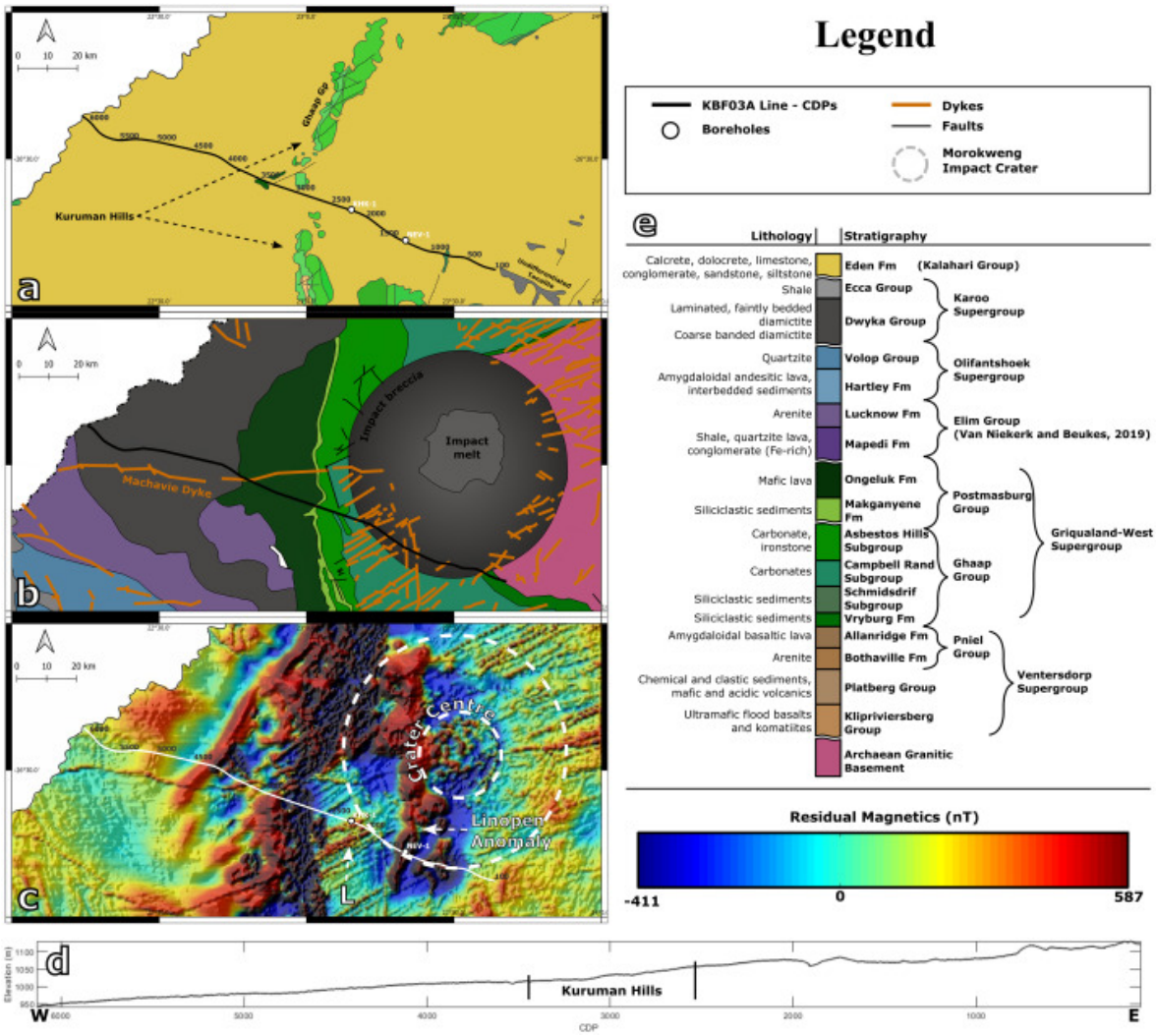

Fig. 2. Surface geology (a), pre-Kalahari (b), and magnetic (c) maps of the region around the KBF03A line, as well as an elevation profile of the line (d). Datasets courtesy of the Council for Geoscience (2019) and sub-Kalahari map of Haddon (2004). Also shown is the general lithostratigraphy (e), where gaps represent unconformities (thicknesses are not to scale). The magnetic map was obtained by removing the regional field from the total magnetic intensity map within the region. A major disruption in the profile coincides broadly with lineament L and an ~80 km diameter circle (dashed line) constructed around the inferred centre of the Morokweng impact structure that broadly coincides with changes in the magnetic character of rocks. (Note the obliquity with which the outer rim intersects the profile).

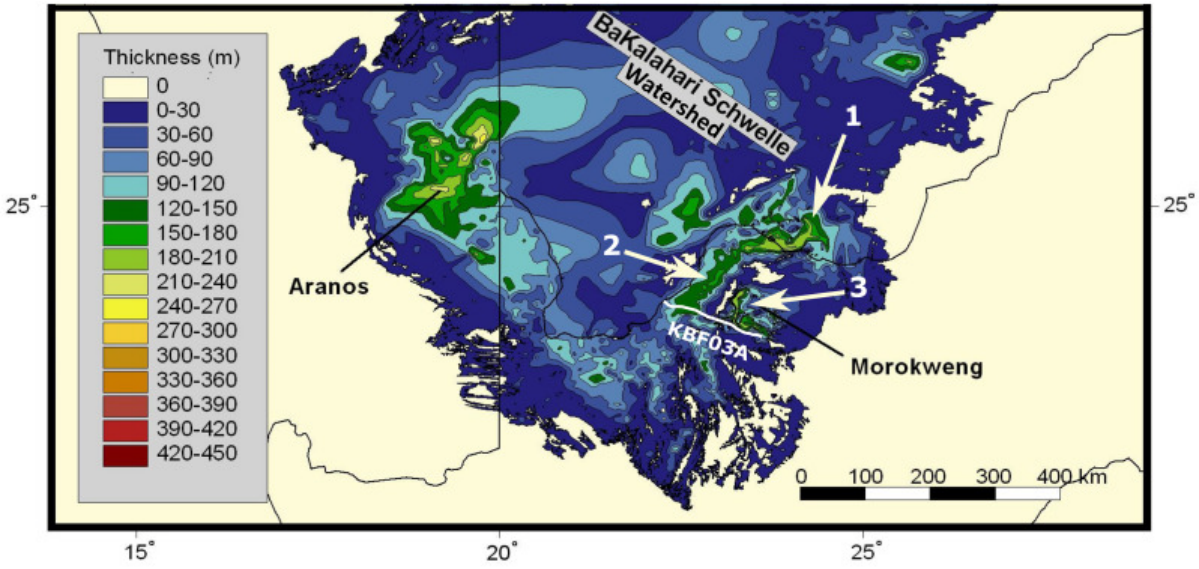

Fig. 3. Isopach map of the Kalahari Group along the border of South Africa and Botswana (after Haddon, 2004), with profile KBF03A superimposed. Areas of localised thickening are labelled 1 to 3.The BaKalahari Schwelle watershed and towns of Morokweng and Aranos are labelled for reference.

The KBF03A profile is located between the towns of Morokweng and Hotazel, extending 150 km WNW to the Botswana border, where it lies across the southern margin of the Kalahari Basin that extends north into central Africa (Fig. 1, Fig. 2, Fig. 3). Within this region, the Kalahari Group has an average thickness of 50–100 m, locally reaching a maximum of ~200 m (Haddon, 2004; Haddon and McCarthy, 2005). It comprises primarily siliciclastic sediments, ranging from conglomerate and sandstone to clayey siltstones, with significant calcrete, silcrete and ferricrete horizons (Haddon and McCarthy, 2005; Partridge et al., 2006). Outcrop is generally poor and much of the stratigraphy and the nature of the underlying basement are known only from a plethora of water boreholes, as well as scarce exposures in stream beds and open cast mines (e.g. Haddon, 2004).

The age of the Kalahari Group is the subject of considerable debate. Previously, Partridge and Maud (1987), Haddon and McCarthy (2005) and Partridge et al. (2006) proposed that the deposition of the oldest, gravel-rich Wessels Formation commenced in local basins between 80 and 100 Ma ago due to the interruption of regional drainage systems by basin warping. These authors also considered that sedimentation in the Kalahari basin continued throughout the Cenozoic without recognizable hiatuses up to the deposition of the unconsolidated cover sand, that Thomas et al. (2000) and Bateman et al. (2003) dated by the optically stimulated luminescence (OSL) method to 300–500 ka. More recently, however, cosmogenic isotope dating of the Boudin Formation that overlies the Wessels Formation revealed that deposition of the former occurred rapidly at 1–1.2 Ma (Gabrielli, 2007; Matmon et al., 2015; Vainer et al., 2018a, Vainer et al., 2018b).

A regional isopach map of the southern Kalahari Basin (Haddon, 2004) shows three areas of localised thickening of the Kalahari Group (Fig. 3). Maximum thicknesses of ~200 m occur in an elongate *E*-W depocentre along the border between South Africa and Botswana. This is linked to a second, NE-SW-trending depocentre with thicknesses up to ~150 m that extends SW towards the western end of the KBF03A profile. The third depocentre defines a narrow crescentic trough up to 200 m deep that lies immediately north of the profile line and

corresponds to the western and southern portions of the Morokweng impact structure (Fig. 1, Fig. 3), as discussed in detail later. More recently, the discovery of the Trans-Tswana river course connecting the Quaternary beds in the study area to the Angolan Highlands has provided additional evidence of the greater tectono-stratigraphic complexity in the Kalahari Group (Vainer et al., 2018b).

Apart from analysis of chips from percussion drilling, the pre-Kalahari Group basement geology has been further inferred from interpretation of regional gravity, magnetic and seismic studies (e.g. Corner et al., 1997; Tinker et al., 2002; Haddon, 2004). In the vicinity of the profile it comprises Neoarchaean granitoid gneisses and subsidiary greenstones onto which a series of supracrustal sequences were deposited. These supracrustals span in age from the Neoarchaean Ventersdorp Supergroup to the passive-margin-type Palaeoproterozoic Griqualand West and Olifantshoek supergroups, all of which dip gently westwards (Tinker et al., 2002; Haddon, 2004). Although there is some doubt as to the stratigraphic subdivisions of the Proterozoic sequences, outcrops to the south and west of the profile indicate that they were subjected to a broadly east-verging, thin-skinned, fold-thrust belt tectonism that affected the western edge of the Kaapvaal craton between ~1.85 and 1.2 Ga (Van Niekerk and Beukes, 2019). This has relevance for the location of the western edge of the craton, which is placed by Van Niekerk and Beukes (2019) approximately 200 km west of the western end of the KBF03A profile, which they termed the Kalahari Line, running between the Kheis Belt and the Kaaien Terrane (Fig. 1). Regional potential-field geophysical data and rare outcrops show that both the granite-greenstone basement and the Neoarchaean-Palaeoproterozoic supracrustal sequences are intruded by multiple dyke sets, mostly of mafic composition, with the most prominent being the 1.92 Ga, ENE-trending, Tsineng dyke swarm (Alebouyeh Semami et al., 2016).

The Carboniferous to Jurassic Karoo Supergroup in the vicinity of the KBF03A profile is restricted to the basal, glacially-deposited Dwyka Group, although the overlying Ecca and Beaufort groups are known to suboutcrop beneath the Kalahari Group west of the Botswana border (Visser, 1982; Key and Ayres, 2000). Regional palaeoenvironmental reconstructions based on the nature and distribution of the Karoo Supergroup lithologies in South Africa, Botswana and Namibia indicate that the KBF03A profile cuts obliquely across the NW flank of a broad flexural arch, known as the Cargonian Highlands, that separated the main Karoo Basin to the south from the so-called South Kalahari Basin (not to be confused with the more extensive Cretaceous-Cenozoic basin) in Botswana and Namibia (Visser, 1982, Visser, 1987). In the context of the interpretation of the main Karoo Basin as a retroarc foreland basin lying north of the Permo-Triassic Cape orogenic system, the Cargonian Highlands are considered to represent the foreland bulge, and the South Kalahari Basin as the back-bulge region (Catuneanu, 2004; Isbell et al., 2008). The Dwyka Group underlying the western edge of the KBF03A profile has been interpreted as the remnants of glacial palaeovalley deposits formed in the Cargonian Highlands during SW to WSW ice flow into the marine depocentre to the west (Visser, 1982; Bangert et al., 1999; Opdyke et al., 2001; Catuneanu, 2004; Catuneanu et al., 2005; Isbell et al., 2008).

A further significant regional feature largely known only from potential-field geophysics, percussion chips from water wells, and exploration borehole cores is the 146 ± 2 Ma Morokweng impact crater (Hart et al., 1997; Koeberl et al., 1997; Kenny et al., 2021). Impact-melt rock has been recovered in boreholes from an approximately 30 km wide area that coincides with a circular magnetic anomaly (Fig. 2c, inner ring) that is interpreted as only the central part of a larger crater. The impact-melt rock is directly overlain by the

Kalahari Group, indicating significant post-impact erosion, estimated at ≥1 km (Wela, 2017). This hampers determination of the original crater size, however, geophysical evidence of suppressed magnetism affecting the prominent Tsineng dyke swarm in an annulus around the melt sheet region (Fig. 2c, outer ring) suggests a minimum diameter of 70–80 km (Koeberl et al., 1997; Henkel et al., 2002). At such a diameter, the KBF03A profile lies across the SSW edge of the impact structure. Potential-field geophysical data show a prominent *E*- to ENE-trending dyke that cuts - and therefore postdates - the impact structure (Machavie Dyke, Fig. 2). It is unclear if this dyke, which also cuts the profile, is related to other broadly E-trending dolerite dykes identified by Key and Ayres (2000) in the Karoo Supergroup suboutcrop west of the profile.

3. Surface geology and geophysics of the KBF03A profile

The surface geology, pre-Kalahari geology and the local magnetic intensity of the area around the KBF03A profile are shown in Fig. 2a, b and c, respectively. Topographically, the profile increases in elevation from ~940 m.a.s.l. (metres above sea level) to 1130 m.a.s.l. towards the ESE (Fig. 2d). The profile transects a gap in the most significant topographic and outcrop feature - the Kuruman Hills (Fig. 2a) - which trace the arcuate outcrop of the gently west-dipping banded iron formations (BIF) of the Kuruman Formation of the Palaeoproterozoic Griqualand West Supergroup (GWS), producing a strong magnetic signature that dominates the magnetic map (Fig. 2c). The eastern end of the profile terminates in the vicinity of scattered small outcrops of Neoarchaean granite and a single outcrop of the basal Vryburg Formation of the GWS (Fig. 2a; Gabrielli, 2007). Apart from this the profile is devoid of outcrops.

The Neoarchaean granitoids at the eastern end of the profile correspond to the southern edge of the broad gravity low known as the Ganyesa Dome, which is interpreted as uplifted basement (Andreoli et al., 1996; Corner et al.,1997; Henkel et al., 2002). Apart from the circular anomalies linked to the Morokweng impact structure and the mainly ENE-trending magnetic lineaments interpreted as 1.92 Ga Tsineng dykes, this basement displays a slightly sinuous, 100 km × 20 km elongate-elliptical, N-trending, magnetic high, informally referred to as the Linopen anomaly (Fig. 2c), that is interpreted as a greenstone belt. This belt tapers southwards towards the KBF03A profile and intersects it at the location of a shallow exploration borehole (NEV-1, Fig. 2c) that records vertical banded ironstone in faulted contact with overlying GWS carbonates (Reimold et al., 2002). The Machavie dyke, which intersects the profile at CDP 3700, cuts the Morokweng impact structure and the ENE-trending Tsineng dykes, indicating a < 146 Ma age, although no sample material has been retrieved to confirm its composition.

The central and western segments of the profile cross a broad sequence of slightly sinuous, NNE-trending magnetic anomalies that include the banded ironstones of the Kuruman Formation. These magnetic anomalies are truncated towards the western edge of the profile by a major NE- to NNE-trending feature to the west of which the magnetic anomalies are more subdued. This 250 km long anomaly coincides with a major W-dipping structural discontinuity in the Palaeoproterozoic basement that Tinker et al. (2002) named the Moshaweng fault. However, whereas Tinker et al. (2002) interpreted displacement on the fault as normal (albeit with possible strike-slip reactivation as well), Beukes et al. (2019) concluded that further north it displaces the Palaeoproterozoic Molopo Farms Complex and its hanging- and footwall lithologies in a reverse sense. The observation that the Moshaweng fault coincides with a distinct change in the pattern of the basement magnetic anomalies

(smoother to the west vs. sharper to the east) strongly suggests that the Dwyka Group is limited to the western side of the Moshaweng fault. Surface exposures and suboutcrops of the Karoo Supergroup are currently unknown to the east of the Kuruman Hills (Haddon and McCarthy, 2005; Gabrielli, 2007; Westgate, 2020), but close to the western end of the profile, in Botswana, the Dwyka rocks are extensively overlain by younger Karoo Supergroup sediments attributed to the Ecca and Beaufort groups (Key and Ayres, 2000; Haddon, 2004).

4. Methodology

The principal aim of this study is to investigate whether reprocessing of the legacy KBF03A seismic profile using modern algorithms and methods allows constraints to be placed on the recent tectonic history of the Kaapvaal craton, which is poorly understood within the interior of southern Africa. Since the acquisition of this profile in 1994, the authors have gained experience in hard rock seismc processing, and more data (mainly magnetic and borehole data) have been made available to constrain the seismic interpretation. Reprocessing involved initial retrieval and recovery of the raw shot gathers, pre-stack processing and application of post-stack processing and migration to correctly enhance the mapping of reflections in space. Subsequent utilization of seismic attribute analysis was done to enhance the subtle structural details within the reprocessed data. In general, reprocessing of the seismic data has resulted in substantially better imaging of the stratigraphy and structural features along the seismic profile, particularly of the unconformities at the bases of the Kalahari and Dwyka groups.

The raw shot gathers and unmigrated stacked data (processed by the contractors in 1994) were received in SEG-Y format. Information regarding the acquisition parameters was obtained from the field observers' reports provided by the company as well as the SEG-Y headers. However, no information is available regarding the original processing workflow for the 1994 stacked section, which was interpreted by Tinker et al. (2002), who concluded that the Dwyka and Kalahari groups were poorly imaged by the data. In addition to the work by Tinker et al. (2002), two boreholes (KHK-1 and NEV-1, see Reimold et al., 2002, Fig. 1) located along the profile, as well as water boreholes studied by Smit (1974), reveal an absence of Dwyka Group sediments along the eastern half of the profile.

4.1. Acquisition

Table 1 details the parameters used for acquisition of the data in 1994. The seismic profile has a total of 3130 shot records (already cross-correlated) with 120 channels per shot and 50 m shot and receiver spacing, and was acquired using the roll-along acquisition method. The resonant frequency of the receivers was 10 Hz (vertical single component) with a low-cut analogue filter of 3 Hz. The resulting nominal CDP fold is 60 and the average CDP fold using the crooked line geometry shown in Fig. 2 is 50 with a bin size of 25 m parallel to the profile. The seismic survey was designed with a sweep length of 16 s and sweep frequency of 15–75 Hz, and a receiver sampling rate of 4 ms. The recorded sweep was cross-correlated with the Vibroseis pilot sweep for each shot location and the correlated trace was saved in a SEGD format and converted to SEG-Y format for processing, the same state that we received the data in. We then investigated the quality of the recorded gathers before setting up the geometry of the profile for reprocessing.

Table 1. Acquisition parameters of seismic line KBF03A.

Survey Parameters	
Type of survey	2D crooked line
Year	1994
Profile length	150 km
Trend	SES-NWN
Split spread	2975–25–X–25–2975 (m)
Nominal fold	60
Recording System	
Recording device	Sercel 338
Sampling rate	4 ms
Record length	6 s
Sweep length	16 s
Sweep frequencies	15–75 Hz linear
Source Information	
Source spacing	50 m
Source type	4 Pelton MK II vibrators in a line
Receiver Information	
Receiver spacing	50 m
Geophone type	10 Hz (SM4U)

4.2. Data reprocessing

A summary of the reprocessing steps applied to the data is given in Table 2. The crooked nature of the seismic profile complicates the seismic imaging quality (e.g. Adam et al., 1998). For example, if the crooked geometry at the NW end of the profile is not carefully considered in the processing stage, steeply dipping reflectors will not be imaged in the final stacked section owing to poor alignment of reflection events in common depth point (CDP) gathers. Considerable success has been achieved through different processing approaches in improving 2D crooked-line imaging in the hard rock environment, especially at crustal scale. Several possible solutions to improve crooked-line imaging are documented in the literature (e.g. Kim et al., 1992, and Nedimović and West, 2003). Given that the profile KBF03A approximates a straight line, the method we decided to use was the standard crooked survey line. This was done by fitting a spline curve through the cloud of common midpoints on the surface with the highest number of binned traces.

Table 2. Processing sequence of seismic line KBF03A.

1.	**Geometry and CDP binning**
2.	First break picking
3.	Trace editing
4.	Amplitude Recovery AGC window length: 500 ms
5.	Floating datum static corrections Fixed datum elevation: 1140 m Replacement velocity: 6000 m/s
6.	Refraction static corrections RMS error < 8 ms
7.	Frequency filtering Notch filter: 50 Hz Bandpass: 5–15–75-100 Hz
8.	F-K filtering F-K mute rejecting velocities below 3100 m/s

9.	Predictive deconvolution Average prediction gap: 30 ms (range of 26–40 ms) Average operator length: 100 ms (range of 80–130 ms)
10.	Velocity Analysis
11.	NMO correction Stretch mute: 60%
12.	Residual statics Repeat NMO corrections and residual statics (3 iterations)
13.	DMO
14.	Stack
15.	F-X deconvolution
16.	Migration Kirchhoff migration velocity: 5500 m/s Maximum allowed stretch: 50%

Fig. 4 shows examples of the recorded shot gathers before and after the initial processing detailed in Table 2. In general, the quality of the data is good, with clear first breaks (indicated by red arrows in Fig. 4a) observed in most of the shot gathers, as well as reflections (indicated by green arrows in Fig. 4). Amplitude spectral analysis of raw gathers indicates that raw data contain the expected frequency range of 10–75 Hz. After binning the traces into CDP bins and merging the geometry with the trace headers, first arrivals were picked in the shot gathers to correct for the effect of low-velocity wave propagation in the overburden (refraction static corrections). Bad traces were then muted and an AGC with a window length of 500 ms was applied to the gathers to recover attenuated amplitudes. Overall, approximately 375,600 first breaks were picked with a preliminary automatic method followed by a precise manual investigation to fine-tune the picked arrivals. Both floating datum statics and refraction statics were applied to the data. The profile had minimum and maximum elevations of 940 m and 1133 m, respectively, and therefore a reference datum elevation of 1140 m was chosen along with a replacement velocity of 6000 m/s, as was determined by analysis of far offset first arrivals. The refraction static corrections were computed using the Generalised Linear Inversion method developed by Woodward (1992) for the first arrivals, inverting for the weathered layer velocity and thickness along the profile. The resulting RMS error was less than 8 ms and the weathered layer exhibited velocities ranging from 2000 to 3500 m/s.

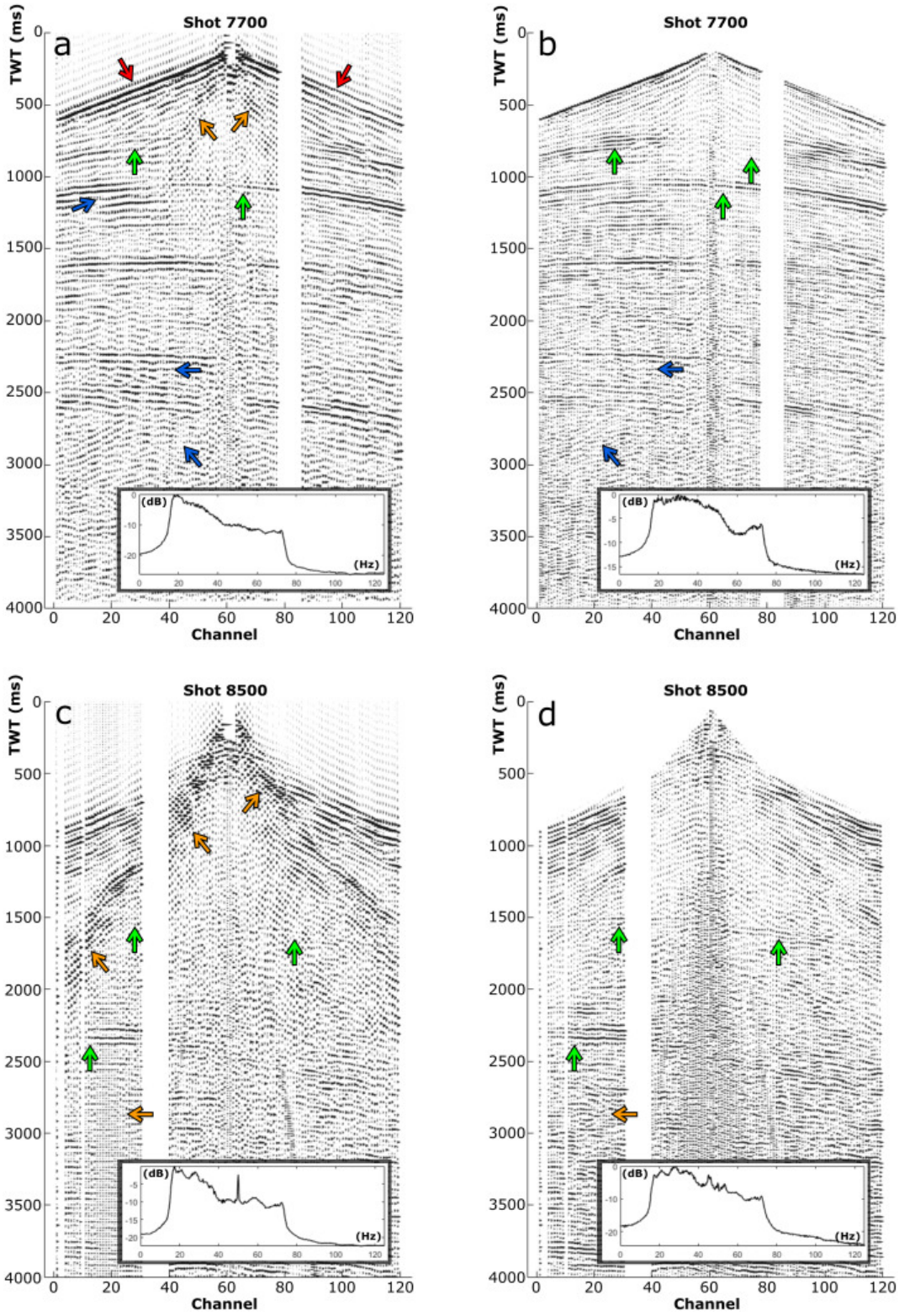

Fig. 4. Comparison of two shot gathers (pairs a, b and c, d) both before (a and c) and after (b and d) applying the pre-stack processing flow described in Table 1. Green arrows indicate enhanced reflections, blue arrows indicate suppressed multiples, red arrows indicate first breaks, and orange arrows indicate noise (including ground roll, air wave and 50 Hz noise likely caused by AC power lines) that has been attenuated. The raw gathers have had a 1 s window AGC applied. Frequency spectra are shown as well.

Prestack processing comprised frequency filtering, f-k filtering and predictive deconvolution. A notch filter was used to remove a dominant 50 Hz component of the data, as indicated by the lowermost orange arrows in Fig. 4c, d, likely attributable to the presence of power lines carrying AC current near certain regions of the survey. A bandpass filter was then applied to attenuate frequencies not contained in the sweep (i.e. 15–75 Hz). From shot-gather analysis, the direct s-wave arrival was determined to have an average velocity of 3100 m/s, thus an f-k mute was applied to remove any linear signal having a velocity less than 3200 m/s (or dip more than 16 ms/trace). Finally, a shot-dependent predictive deconvolution was applied with the prediction gap and operator length being specified every hundredth shot and interpolated for intermediate shots. Hence the deconvolution parameters varied across the length of the profile; the prediction gap had an average of 30 ms and ranged from 26 ms to 40 ms and the operator length had an average and range of 100 ms and 80 ms to 130 ms, respectively.

As indicated by the green arrows in Fig. 4, reflection continuity and temporal resolution are considerably enhanced by deconvolution and frequency filtering. The deconvolution also suppressed short-wavelength reflection multiples, as indicated by the blue arrows, and there has been significant noise reduction and signal boosting owing to the notch and f-k filtering. The 50 Hz noise can be seen in the left region of Fig. 4c from 2 s downwards (orange arrow), which has been suppressed by the notch filter in Fig. 4d. Muted traces were already present in the raw data.

Detailed velocity analysis was performed using constant velocity stacks to generate a velocity model for dip-moveout (DMO) corrections. Prior to DMO corrections, careful residual static corrections (consisting of three iterations) were applied to increase the coherency of the reflections. The DMO velocity model was chosen to ensure the imaging of both shallow and deep, steeply dipping reflections. The final DMO velocity model exhibited values from 3000 to 6500 m/s (the lower velocity values of 3000 to 4000 m/s are attributed to the Kalahari and Karoo sediments). An offset-time Kirchhoff dip-moveout (DMO) was then applied to the data, followed by stacking of the data along the CDP line with a 60% stretch mute. F-x deconvolution was applied to the stacked section to increase signal-to-noise ratio of the data by boosting coherent events. Several migration algorithms (e.g. Stolt, finite difference, phase shift and Kirchhoff migration methods) were tested for poststack migration. After several tests, the stack was migrated using a frequency-domain Kirchhoff migration (Yilmaz, 2001) as it resulted in the best images.

5. Results and interpretation

5.1. Imaging of Phanerozoic sediments

Fig. 5 shows the results of the reprocessed and interpreted section of profile KBF03A. The focus of the interpretation comprises the Dwyka and Kalahari groups and the section has thus been truncated at 650 ms and features exclusive to the underlying Proterozoic metasediments, which are the subject of a separate study, have been are not discussed in detail In general, both the Kalahari and Dwyka unconformities exhibit strong reflections that are disrupted by structural features including faults and folds.

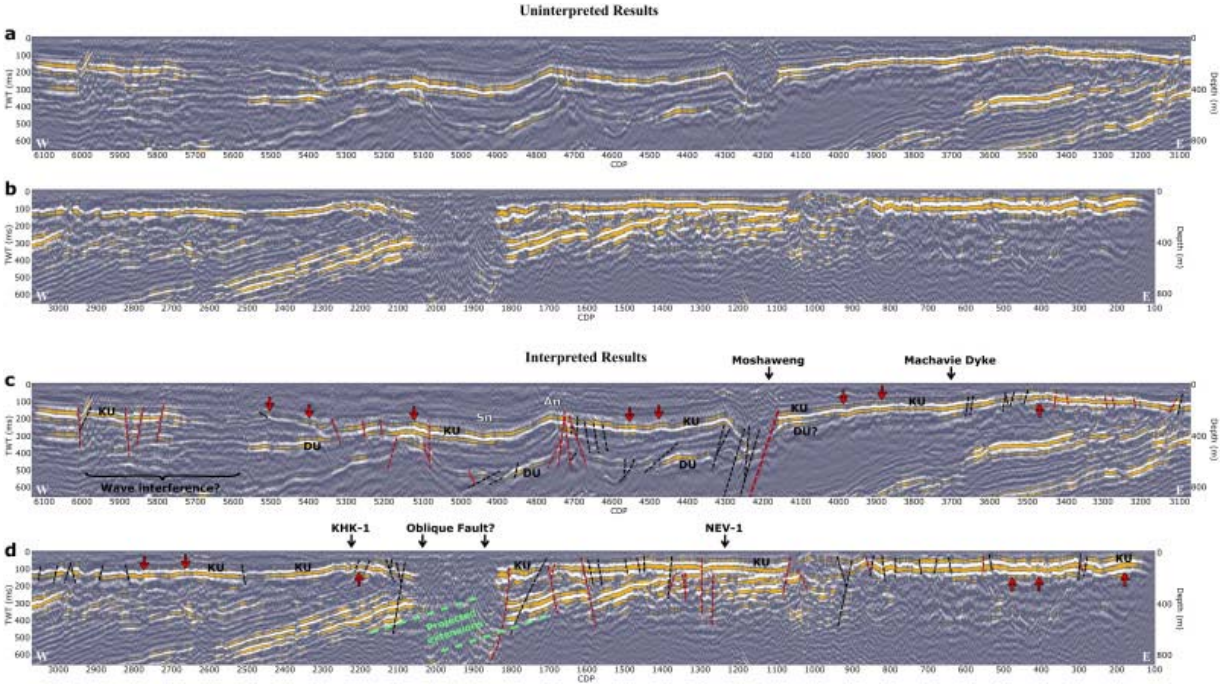

Fig. 5. Top 650 ms of the fully reprocessed seismic profile. The western half (a) runs from CDP 6100 to CDP 3100 and the eastern half (b) runs from CDP 3100 to CDP 100. Interpretations made along the profile are exclusive to the Kalahari and Dwyka unconformities (KU and DU, respectively). Black lines and red lines are indicative of reverse/thrust and normal faults, respectively, and red arrows denote folding. An: Antiform; Sn: Synform. The locations of boreholes KHK-1 and NEV-1 (see Reimold et al., 2002) are plotted along the profile.

In particular, the western end of the profile (CDP 4000–5100), where the Dwyka Group suboutcrop is present, reveals broad (~10 km wavelength) cofolding of both Kalahari and Dwyka sediments, with notable anticlinal (An) and synclinal (Sn) features (Fig. 5). The Moshaweng fault is located near CDP 4200, where it appears to truncate the Dwyka Group and severely disrupt the Kalahari Group. East of the Moshaweng fault, the Kalahari Group exhibits multiple folds of varying wavelength as well as faulting, with two distinct discontinuities that disrupt the Kalahari unconformity reflection entirely. The first, located between CDPs 1800 and 2100, is void of any reflections from both Phanerozoic and Proterozoic layers. We interpret this region as the possible intersection of the seismic profile with a highly oblique fault zone, owing to its ~5 km expanse (Fig. 5). The second major zone of disruption is located between CDPs 900 and 1000 and is characterised by chaotic reflections. These features and their neotectonic implications are discussed in more detail in the *Structural Interpretation* and *Discussion* sections.

5.2. Seismic tomography

A first break travel time tomography up to a depth of 1200 m, which accounted for elevation, was computed using picked first breaks across the entire profile (maximum offset in shot gathers was ~3000 m). The velocities and ray paths are displayed in Figs. 6a and b, respectively, as well as traces overlaying the velocities and an interpreted section in Figs. 6c and d, respectively. The interpreted section merely shows proposed low-resolution velocity boundaries between strata, with faults other than the primary Moshaweng fault not shown. The tomography shows that the seismic velocities of the Kalahari Group sediments range between 1000 m/s and 3500 m/s, reflecting its variable lithification, whereas the Dwyka

Group sediments range between 3000 and 4000 m/s. The underlying crystalline Proterozoic and Archaean lithologies have velocities larger than 5000 m/s and are clearly imaged by the tomography. These velocity values correlate with the sonic logs of the KHK-1 and NEV-1 boreholes (Reimold et al., 2002) in the eastern part of the profile, as interpreted by Anglo American Corporation, as well as those reported by Tinker et al. (2002), as velocities from the latter two studies fall within the quoted velocity ranges from the tomograms.

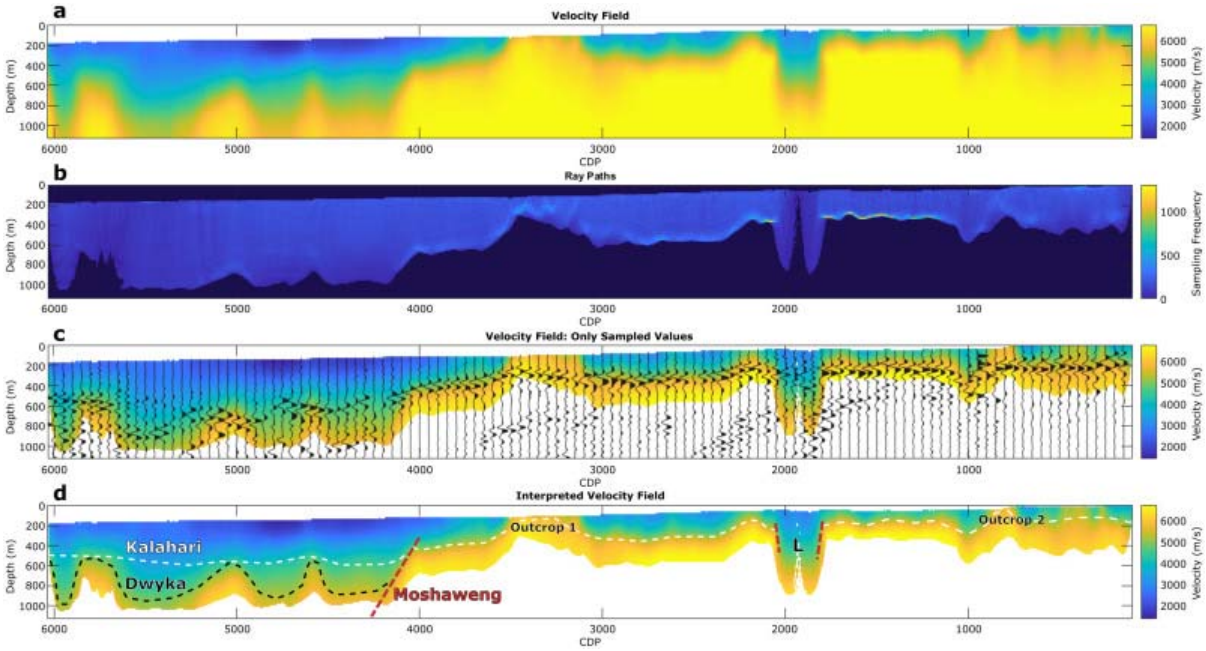

Fig. 6. First-break traveltime tomogram of seismic line. The velocities are displayed in (a), the ray paths in (b), and a composite in which only velocities that were sampled by at least one ray path are kept. The composite is displayed with every 50th trace of the stack overlaid in (c), as well as with a basic interpretation of the tomogram in (d). "L" in d corresponds to the location of the magnetic lineament of the same label in Fig. 2c.

The ray paths, shown in Fig. 6b, sample the sediments of the Dwyka and Kalahari groups effectively, with as many as 1200 ray paths coinciding along the sediment interfaces. Most ray paths were refracted at the boundary separating the Phanerozoic sediments and Proterozoic metasediments, providing a good proxy of where this boundary lies and improving confidence in the reflection interpretation. Fig. 6c demonstrates good correlation between the refraction velocity model and the reprocessed stack. In this figure, every 50th trace is overlaid on the velocity model. There is strong correlation of the Kalahari Group unconformity along most of the profile. The Dwyka Group unconformity also correlates well with the reflection seismic section (Fig. 6d) and is constrained to a depth between 400 m to 800 m, exhibiting low velocities <4000 m/s.

The interpreted tomography is shown in Fig. 6d. As previously mentioned, the interpretation is of first-order features only, and indicated boundaries are based on velocity differences and do not resolve faulting and short wavelength folding. Two outcrops of Archaean-Proterozoic rocks are evident on the tomography near CDPs 1000 and 3500; these are visible on the geological map (Figs. 2a and 6d).

At CDP 2000 in Fig. 6d, labelled "L", the ray paths are severely disrupted, have no distinct boundary and travel to a significant depth, indicating a low velocity zone with an

undetermined lower boundary. The profile intersects, and is highly oblique to, two features at this point that are visible in the potential field geophysics, namely, a prominent magnetic lineament ("L" in Fig. 2c) and the outer parts of the Morokweng impact structure (Fig. 2b,c). These are discussed further below.

5.3. Comparison between legacy data and reprocessed data

The seismic section down to 1.5 s TWT exhibits similar first-order features to that of Tinker et al. (2002), with the Dwyka Group underlying the Kalahari Group to the west of the Moshaweng fault, which is at CDP 4200, and the Kalahari Group unconformably overlying progressively older Proterozoic to Archaean rocks towards the east (Fig. 7). However, the reprocessed data have significantly enhanced both unconformities, revealing their more precise location and, thus, better depth constraints and better resolution of finer structural detail that was not apparent in the legacy dataset.

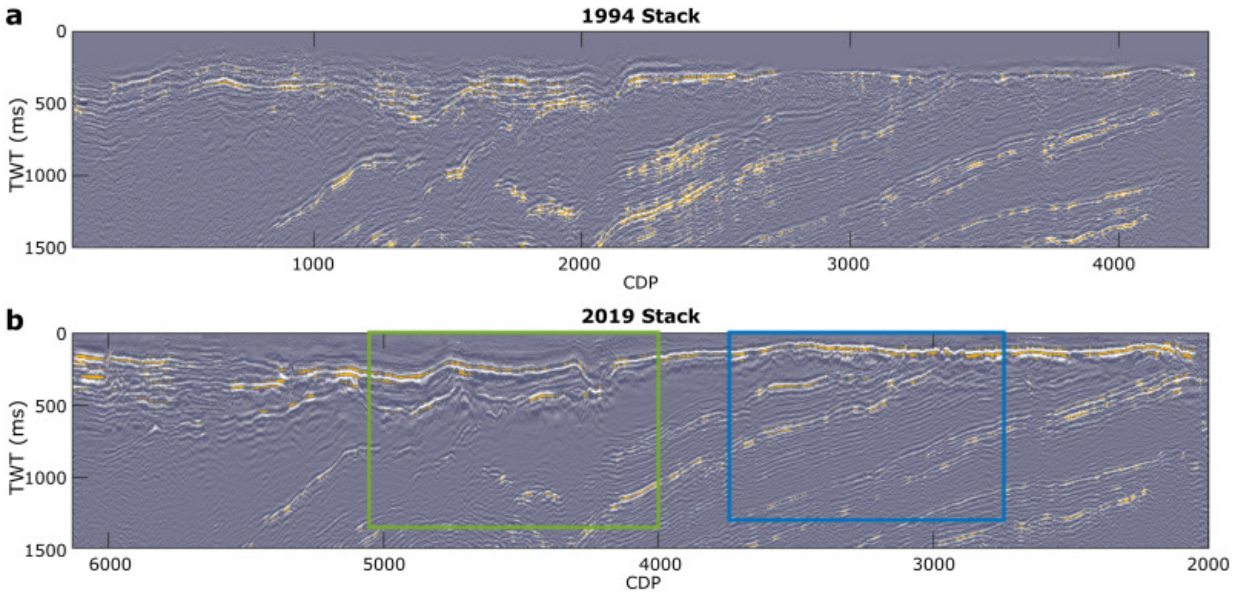

Fig. 7. Comparison of legacy stack section (a) with reprocessed stack section (b). Regions of notable improvement are outlined in rectangles and corresponding zoomed sections are shown in Fig. 8. Note that CDP labels are different for the two datasets as our CDP bins increased from east to west (following direction of acquisition).

As the migrated legacy data were unavailable, the legacy unmigrated stacked section is used for comparison with the reprocessed unmigrated stacked section, as shown in Fig. 7, Fig. 8. Fig. 7 comprises the majority of the profile and Fig. 8 comprises zoomed windows of both the legacy stack and the reprocessed stack. Fig. 7 is truncated at 1.5 s TWT for better display and because most improvements in the data are evident within this window. There are a few prominent differences between Figs. 7a and b, which are examined in more detail within the coloured rectangles in Fig. 8.

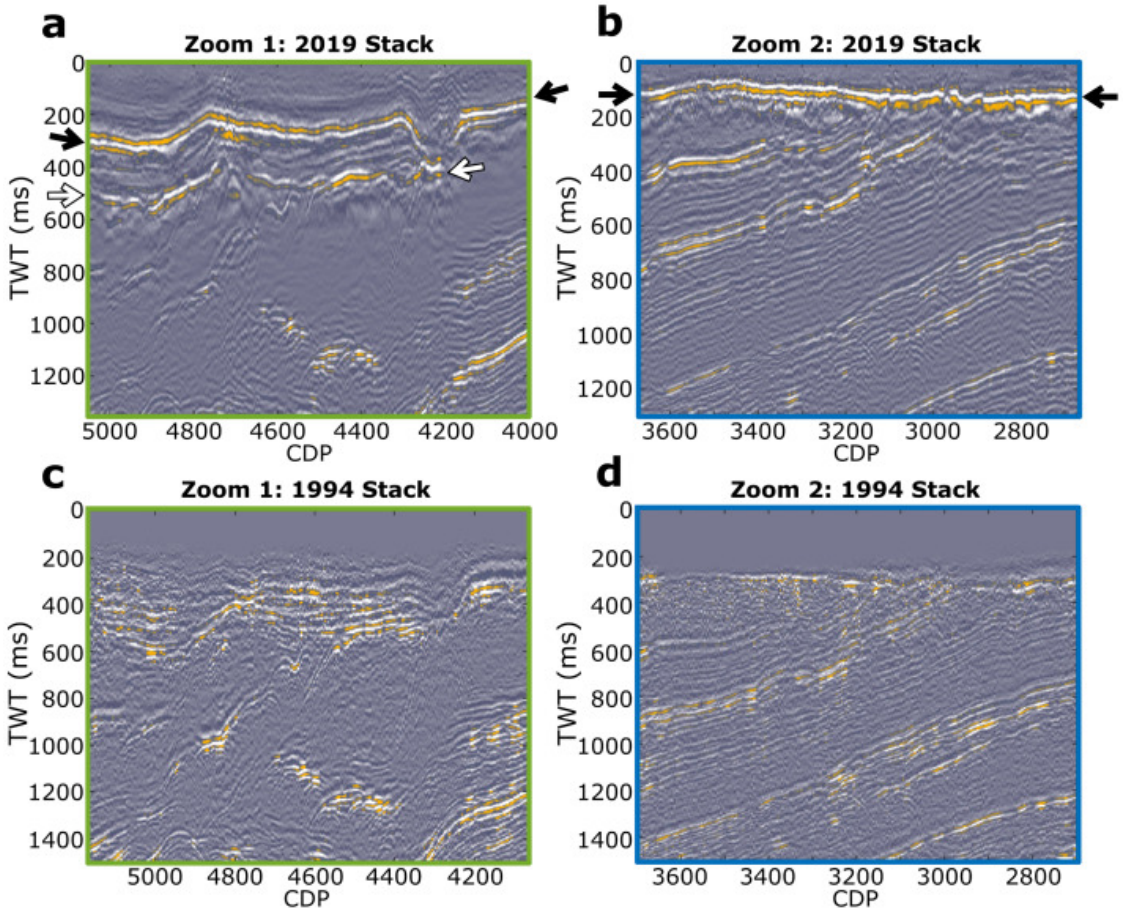

Fig. 8. Zoomed regions of reprocessed stack (a and b) and corresponding regions of old stack (c and d). The colours of the outlined boxes correspond to those shown in Fig. 7. White arrows indicate Dwyka unconformity reflections and black arrows indicate Kalahari unconformity reflections.

Figs. 8a and b clearly delineate the base of the Kalahari Group (black arrows), which was poorly imaged in the 1994 stack (Figs. 7c and d). In the 1994 data, the overall signal-to-noise ratio is poorer, preventing the reflections from being clearly imaged and blurring the junction point of the dipping layers and the unconformity west of the Moshaweng fault. Additionally, the Dwyka unconformity (white arrows), while still discontinuous, exhibits an evident improvement in the reprocessed section relative to the 1994 stack. Finally, while the Proterozoic sediments underlying the two unconformities are not the focus of this study, it is worth noting their improvement in image clarity after reprocessing, as shown by the clearer parallel, dipping reflections in Fig. 8b compared to Fig. 8d. Replication of faults and folds in the reprocessed data is promising and strengthens the confidence of our proposed interpretation as discussed later in the paper. For example, the faults seen in the dipping layers of Fig. 8b match those of the legacy data in Fig. 8d. Coupled with the enhancement in reflection continuity, these replicated features are more likely to be the result of geological features and not computational or interpretive artefacts.

5.4. Seismic Attributes

To further improve and enhance the mapping of geological features, we applied seismic attributes to the reprocessed seismic section. Instantaneous seismic attributes were first

introduced by Taner et al. (1979) and have since proven invaluable as seismic interpretation techniques to enhance the structural interpretation of seismic data (Taner et al., 1979; White, 1991; Brown, 1996; Barnes, 2000). The two core instantaneous attributes - the instantaneous amplitude *A(t)* and instantaneous phase *φ(t)* - are derived from the complex trace *c(t)*, associated with the original trace *s(t)*, as follows:

$$c(t) = s(t) + iH[s(t)]$$

$$A(t) = |c(t)|$$

$$\varphi(t) = \arg\{c(t)\}$$

where *H[]* is the Hilbert transform and *arg{}* is the complex argument, or angle. The cosine of the instantaneous phase, *cp = cos(φ(t))*, is typically used as an attribute instead of the phase itself. The instantaneous amplitude attribute is useful at highlighting strong reflections as it is a measure of the local absolute amplitude of the wavelet. The instantaneous phase, on the other hand, removes all amplitude information and acts as an idealised automatic gain control (AGC). It thus enhances weak reflections and emphasises subtle changes within a reflection across traces, making it useful to pick up vertical features such as faults (Taner et al., 1979).

Westgate (2020) introduced an attribute that is a composite of either of the two above mentioned instantaneous attributes and the novel symmetry attribute (Manzi et al., 2019; Westgate, 2020). The composite attribute is a hue-saturation-intensity (HSI) image that is created by assigning one of the instantaneous attributes to the intensity component of the image and assigning the symmetry attribute to the hue component of the image. The symmetry component, as explained by Westgate (2020), is calculated by running a window through the seismic section of user-defined size and the centre value of the window is calculated to give the local symmetry of the data within that window. The result is a doubling of the wavelet limbs – due to symmetry attaining a maximum at every trough and peak and a minimum at every point of inflection – which adds a layer of detail to the to the wavelet anatomy. Additionally, symmetry is independent of amplitude so it acts both as a gain filter and an edge detector.

The advantages of this attribute, compared to the conventional attributes, are that it is able to enhance both strong and weak reflections while still distinguishing between them, and it is also effective at tracking continuity of reflections in both hard rock and soft rock settings (Westgate, 2020).

Two instantaneous attribute composites have been computed to enhance the continuity of Kalahari Group and Dwyka Group reflections along the section and, thus, for the identification of faults, folds and other structural features along the reflections. The first is a composite of the symmetry and instantaneous phase, which is used to enhance weak reflectors and track continuity. The second is a composite of symmetry and instantaneous amplitude, which is useful for highlighting zones of strong reflectivity and bedding. Fig. 9 shows different sections of the line within the top 800 ms TWT. Such features are evident in the Kalahari Group unconformity in Zoom A and Zoom B of Fig. 9, shown by light and dark blue arrows, with particular attention to the Moshaweng fault in Zoom B, which is more

easily delineated in the symmetry-phase composite. The Dwyka Group sediments also exhibit faulting in Zooms B and C in the composite attributes.

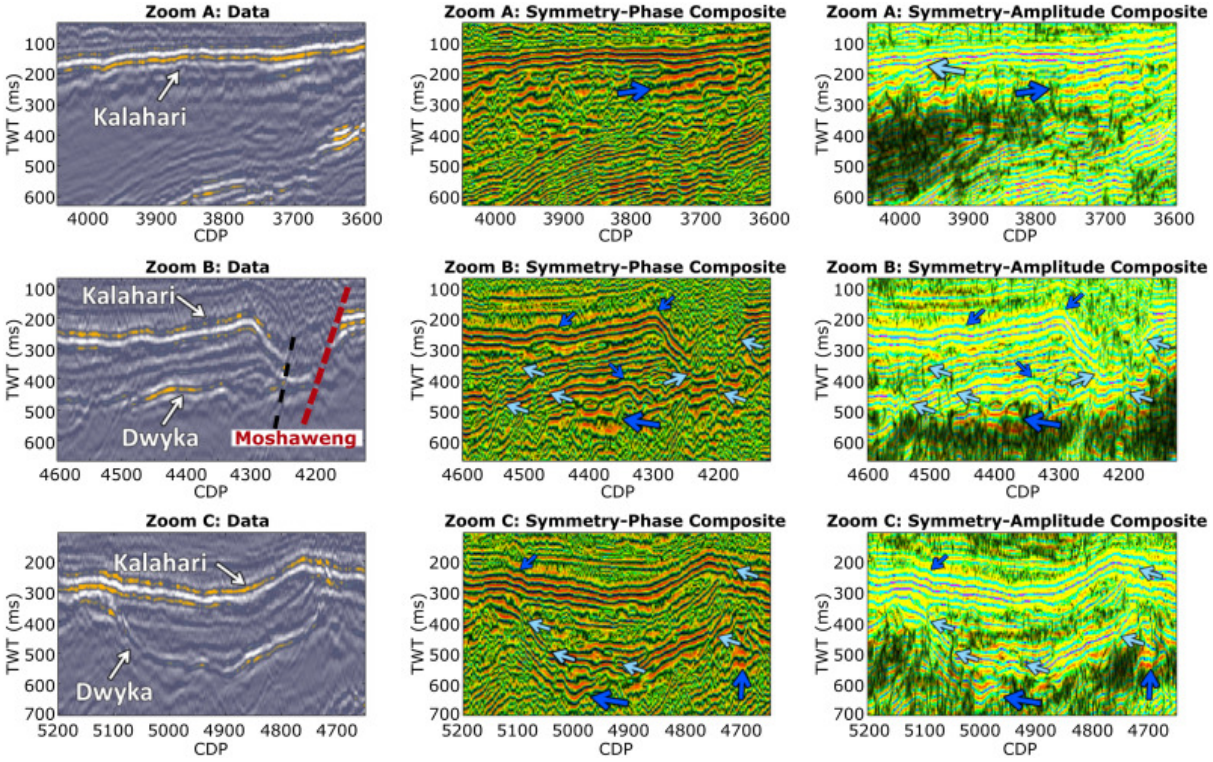

Fig. 9. Attribute analysis: three different sections (Zooms A to C) showing, from left column to right column, the original data, the composite of symmetry and instantaneous phase cosine, and the composite of symmetry and instantaneous amplitude (Westgate, 2020). Light blue arrows indicate faulting, dark blue arrows indicate folding. Red dotted line in Zoom B resembles Moshaweng primary normal fault and black dotted line resembles reverse fault.

These seismic attributes also enhance subtle features in the data owing to their AGC properties, in this case folding features are enhanced. Zooms A and C of Fig. 9 illustrate significant folding in both the Kalahari and the Dwyka sediments (dark blue arrows). Light blue arrows show regions of substantial folding, which manifest in both the Kalahari and Dwyka unconformities.

5.5. Structural interpretation

5.5.1. Kalahari Group

Contrary to Tinker et al. (2002) who suggested that the Kalahari Group unconformity along the length of the profile is seismically transparent, the reprocessing results show a strong reflector over much of the profile length. This has allowed us to more precisely constrain Kalahari Group thicknesses across the profile and to investigate structures affecting it. The Kalahari Group thickens broadly from ESE to WNW along the profile, reaching a maximum thickness of ~250 m at CDP 4910 and at the western edge of the profile (Fig. 5), which is consistent with water borehole percussion drilling data from within the region (Haddon, 2004; Haddon and McCarthy, 2005) (Fig. 3). The shallowing towards the basement outcrops at CDP 3500 and CDP 1000 is evident, as is the slight deepening between CDP 2250 and

CDP 3200 (Fig. 5), which coincides with the southern edge of the crescent-shaped depocentre that corresponds to the outer parts of the Morokweng impact structure, in which maximum thickness approaches 200 m (Fig. 3; Haddon and McCarthy, 2005). The overall deepening across the profile to the WNW is consistent with the incursion of the profile slightly deeper into the Kalahari Basin from the ESE end of the profile, which lies close to the current outcrop limits of the Kalahari Group (Fig. 3).

The continuity of the Kalahari Group unconformity reflections, as seen in Fig. 5, is disrupted at CDP 1850–2050 and across the Moshaweng fault at CDP 4150–4300, and reflections are less well-defined at CDP 950–1050, and CDP 5500–5700, the lattermost of which may be attributed to the kink in the profile geometry within this area (Fig. 2). The ~5.5 km wide disruption at CDP 1830–2050 is unusual as it extends a significant distance into the underlying crystalline basement. Examination of the raw shot gathers within this zone, as shown in Fig. 10, reveals that there are no evident coherent reflections and the first breaks are virtually incoherent, with a strikingly clear disruption in reflections at both ends of the feature, to a degree where the edges of the feature can be precisely pinpointed. The latter suggests that this is not an acquisition defect related to poor geophone coupling or a highly variable weathered layer. Although a major dyke intersects the profile at this zone (L in Fig. 2c), the tomography results (Fig. 6) indicate unusually slow seismic velocities, which seems inconsistent with a dyke of likely mafic composition; furthermore, comparison of the profile with the potential-field image shows no similar effects where other dykes cross the profile (e.g. Machavie dyke at CDP 3700 in Fig. 5) and the dyke in question also appears to be itself disrupted by the projected rim of the Morokweng impact structure (Fig. 2c). Slow seismic velocities and scattering would be compatible with highly faulted rocks (Iacopini et al., 2016). The west-dipping Proterozoic rocks beneath the Kalahari unconformity in this area are disrupted by several faults with significant apparent *E*-side-down normal-slip displacements (Fig. 5). The unconformity itself does not demonstrate a similar magnitude of vertical offset; however, small-scale faults and folds affecting the Kalahari unconformity are more intensely developed immediately adjacent to CDP 1850–2050 compared with the rest of the profile (Fig. 5). From this, we suggest that the disruption in the Kalahari unconformity is linked to faulting that is localised above a zone of basement rocks that were already highly faulted but that did not themselves involve large post-Kalahari Group displacements. Fig. 2 also shows that the profile is approximately tangential to the Morokweng impact structure and, if the ~80 km diameter estimate (Henkel et al., 2002) is correct, the profile appears to cut through the SSW sector of the crater rim, which would be expected to display N- to NNE-side-down block faulting along E-W to ESE-WNW listric N-dipping faults (e.g. Kenkmann et al., 2014). Up-dip projection of the prominent W-dipping GWS reflector lying west of the disrupted zone (Fig. 5) shows that the zone must accommodate a substantial downthrow of the reflector to the east/north. The width of the zone of anomalous signals both above and below the unconformity and the apparent E-side-down displacement of the underlying W-dipping basement strata would both be consistent with an oblique intersection of the pre-Kalahari Group Morokweng crater rim. In this case the true downthrow of the basement fault(s) would have been directed to the NNE, while the thickening of the Kalahari Group isopachs suggests that these pre-Kalahari Group faults underwent subsequent reactivation.

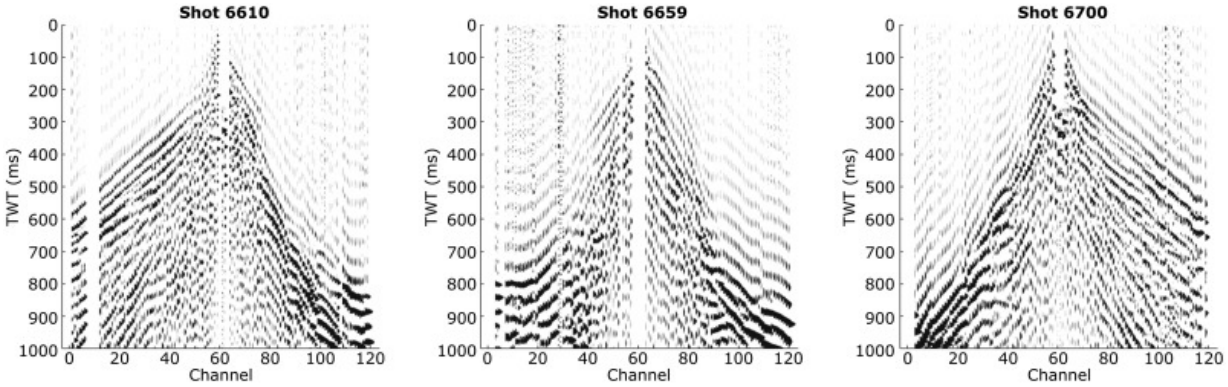

Fig. 10. Shot gathers at either end (shots 6610 to the West and 6700 to the East) and centre (shot 6659) of the major discontinuity centred on CDP 2000, illustrated in Fig. 5. Note the collapse of first breaks within this region, possibly caused by loose overburden, leading to bad coupling.

The weak and disrupted signal at CDP 900–1100 in Fig. 5 could reflect the shallowing Archaean basement rocks, but could also be related to the proximity of vertical N-S-trending Archaean greenstone lithologies that are inferred based on the intersection of the profile with the N-S-trending Linopen magnetic anomaly at this point (Fig. 2b). Gabrielli (2007) identified a small inlier of Archaean greenstone mafic rocks outcropping beneath the Vryburg Formation (lowermost Griqualand West Supergroup) close to the profile. The presence of either Campbell Rand Subgroup dolomite or Archaean granite directly below the Kalahari Group cover within boreholes located at the nearby Melrose farm supports the presence of faults in the vicinity (R. Correns, personal communication, 1996).

A sharp disruption within the Kalahari Group is observed at CDP 6000 (Fig. 5), which is characterised by what appears to be a steeply dipping (>60°) dislocated block. However, the wavelet associated with this feature has a discontinuous phase and is contracted, suggesting that it is an anomalous feature likely due to wave interference (e.g. from out-of-plane reflections).

The Kalahari unconformity is disrupted by multiple faults with varying orientations and apparent reverse - and rare apparent normal - displacements of up to tens of metres (Fig. 5), as well as large-wavelength (>1 km) gentle folds that are generally spatially associated with the faults. The steep overall apparent dips (>60°) of the faults is misleading owing to the vertical exaggeration in Fig. 5; in reality, most faults have apparent dip angles of 10–30°, although true dip direction cannot be constrained from a 2D profile. Fault intensity is higher on the eastern side of the profile, where the Kalahari Group directly overlies Palaeoproterozoic basement that appears to be significantly disrupted, and is especially common between CDP 100 and CDP 2200, within the limits of the Morokweng impact structure (Fig. 2, Fig. 5). As the Kalahari Group unconformably overlies the partially eroded Morokweng impact melt (Andreoli et al., 1996), these faults cannot themselves be impact-related. However, the previously mentioned faults that extend into the basement beneath the unconformity appear to be continuous with faults cutting the unconformity, but have larger senses of throw.

In the western part of the profile where the Dwyka Group underlies the Kalahari Group, faulting of the Kalahari Group appears less intense, with the exception of the immediate hanging wall adjacent to the Moshaweng fault (Fig. 5). However, fault and fold features with a similar general scale and appearance to the Kalahari Group are also observed affecting the

Dwyka Group unconformity. The Kalahari Group unconformity is more strongly disrupted above areas where the pre-Dwyka basement lies closer to the surface (Fig. 5). The most intense faulting with the largest displacements occurs where the Kalahari unconformity shows large-scale anticlinal folding, at CDP 4250 and CDP 4700.

In the vicinity of the Moshaweng fault, the orientation and disruption of the Kalahari unconformity becomes complex. In the footwall east of the fault, several strong reflectors show variable amounts of steepening towards the fault, consistent with normal drag folding on a normal dip-slip fault. In the hanging wall a highly disrupted syncline appears to exist immediately adjacent to the fault between CDP 4200 and CDP 4150 but the unconformity steepens away from the fault between CDP 4300 and CDP 4250, dipping eastwards towards the fault on the limb of a large-scale anticline (Fig. 5). The steepened limb is well picked out by the symmetry-phase composite in Fig. 9. While this feature bears some resemblance to a rollover anticline above a normal dip-slip fault, the crest of the hanging wall anticline defined by the unconformity is at the same approximate elevation as the unconformity in the footwall to the fault (Fig. 5, Fig. 9). The hanging wall anticline is also matched by a similar, slightly less pronounced, asymmetric anticline with an opposing sense of vergence at CDP 4750, and the Dwyka unconformity in the hanging wall of the Moshaweng fault does not appear to be similarly steepened (see symmetry-phase composite in Fig. 9), as would be expected for a rollover anticline. Taken together, and given the common association of folds affecting the unconformity with faults with apparent reverse slip, these features suggest that the fold in the hanging wall of the Moshaweng fault is rather related to compression and, thus, that it formed in association with inversion of an original post-Kalahari unconformity normal fault. This inversion largely reversed the earlier bulk downthrow of the west block of the Moshaweng fault, as discussed further in the *Discussion* section, although localisation of reverse slip west of the principal normal fault plane has preserved evidence of the earlier episode. Based on the reprocessed data, we suggest that the Moshaweng fault manifests as an ~2.9 km wide zone, different parts of which were reactivated at different times during and following Kalahari Group deposition.

The reprocessed data reveal that the Kalahari unconformity is folded on a wavelength from ~1–2 km up to ~10 km. The smaller folds show the most regular wavelengths but are nonetheless highly variable (e.g. CDP 100–550, Fig. 5), commonly intensifying in parallel with the increased prevalence of faults, most of which show apparent reverse slip (e.g. CDP 800). Locally these folds are concentrated, together with faults, in the hinges of larger wavelength anticlines (e.g. CDP 2200 and 3450). In general, the folds appear upright to only slightly asymmetric, although it is not possible to determine the true orientations of structures in a 2D profile, particularly as the Kalahari Group outcrop is extremely limited and of poor quality. Nonetheless, Google Earth image analysis indicates a left-stepping *en echelon* pattern of subparallel, sharp and straight, WNW-ES*E*-trending (110–115°) lineaments in the floodplain of the Moshaweng River towards the eastern end of the profile where some of the most prominent large-scale folds occur (e.g. CDP 800–900). Kilometres-long lineaments in the Kalahari Group exposures in the vicinity of CDP 3200 display a predominant 060° trend, with a spread towards 045°. A broad E-W orientation of the post-Kalahari Group folds and faults would be consistent with similar features observed near Hotazel at the Kudumane Mine (Fig. 1; see Section 6 (*Discussion)*).

The largest fold structures range from relatively concentric gentle anticlines with parasitic folds and broad intervening synclines that are found in the central and eastern parts of the profile (anticlines at CDP 2200 and 3480) to the more angular anticline pair west of the

Moshaweng fault between CDP 4250 and 4750. These latter hinges flank a broad syncline displaying secondary km-scale folds. Based on our interpretation of the underlying Dwyka unconformity and basement structures, we propose that this 7–10 km wide feature represents forced folds above a conjugate pair of reverse faults. The reprocessed data do not appear to support the presence of a large erosive channel feature within the Kalahari Group towards the western edge of the profile between CDP 5800–6100 that was proposed by Tinker et al. (2002).

5.5.2. Dwyka Group

The Dwyka Group is limited to the western third (~45 km) of the profile, with its eastern extremity lying along the Moshaweng fault (Fig. 5). Tinker et al. (2002) inferred a highly irregular basal unconformity, which they attributed to both erosive topography formed by the ice sheet and pre-Kalahari Group faulting, without providing specific details. They interpreted the elevated basement at CDP 5100–5160 as a 150 m high glacial erosive feature and show the Dwyka Group as thickening to ~350 m to the west, with the unconformity reaching a depth of ~600 m below surface at the end of the profile. Based on the reprocessed data, we infer that the Dwyka Group thickness was relatively constant, at ~200 m, across much of the profile. This is consistent with thickness estimates through large parts of the South Kalahari Basin in Botswana (Visser, 1982; Key and Ayres, 2000), west of the termination of the profile. Visser (1982) shows the Khuis Outlet Dwyka as being covered by a minimum of 350 m of Ecca, which would be consistent with deepening of the Dwyka unconformity to the west.

The exceptions to the rule of a relatively constant Dwyka Group thickness occur immediately west of the Moshaweng fault where it thins to a few tens of metres before signal clarity is lost, and at CDP 5100–5160 (Fig. 5). The eastward thinning in the hanging wall of the Moshaweng fault is linked to convergence between the Dwyka and Kalahari unconformities, which would be consistent with rotation of the Dwyka Group by normal drag folding along the fault prior to deposition of the Kalahari Group. An intriguing feature resulting from the improved imaging is the presence of a lower, more steeply west-dipping, reflector beneath the Kalahari Group reflector in the immediate footwall of the Moshaweng fault and that appears to terminate against the latter at CDP 4000 (Fig. 5, Fig. 8a). One possible explanation of this feature is that it represents a remnant of down-dragged Dwyka Group against the fault. Unfortunately, definitive confirmation of such an option is hampered by the thickness of this feature lying close to the tuning thickness of the data, and there is no borehole data to constrain this interpretation; nonetheless, it would be consistent with Beukes et al.'s (2019) observation of small remnants of Dwyka Group in the footwall of the Moshaweng fault north of the profile, and would thus place tighter constraints on the amount of post-Karoo throw along the fault.

Development of a horst block owing to normal-slip faulting with throws of 100–150 m prior to Kalahari Group deposition explains thinning of the Dwyka Group to ~50 m at CDP 5100–5160 (Fig. 5). The change in the magnetic map at CDP 5100 (Fig. 2c) is consistent with raised Proterozoic basement and suggests that these faults have an approximately N-S strike. This interpretation implicitly differs from that given by Key and Ayres (2000) who proposed an erosive relief of >100 m along the Dwyka unconformity. Apart from the large-scale normal block faulting at CDP 5100–5160, the Dwyka unconformity exhibits gentle, km-scale, east-verging folds and low-angle west-dipping faults with apparent thrust displacements of ≤100 m at CDP 4400–4600 and CDP 4850–5000, as well as significant co-folding with the

Kalahari Group (10–20 km wavelength and ~ 300 m amplitude), as seen in Fig. 5. At CDP 4700–4750 both unconformities are folded and faulted; however, the Dwyka unconformity anticline is more severely disrupted by faults than the anticline defined by the Kalahari unconformity (Fig. 5).

6. Discussion

6.1. Resolution of seismic data

Reprocessing the legacy seismic profile KBF03A has yielded a migrated section that is clearer and characterised by a greater signal-to-noise ratio, thus allowing for a refined interpretation. The structural history of the Dwyka and Kalahari groups in the profile is more complex than previously suggested by Tinker et al. (2002), with Karoo and Kalahari sediments exhibiting widespread faulting as well as folding. Our interpretation is reliant on our confidence in the resolution of the seismic data relative to Tinker et al. (2002). The dominant frequency of the final migrated section (Fig. 5) is 35 Hz, yielding a tuning thickness of 40 m (assuming an average medium velocity of 5500 m/s) (Widess, 1973). The lateral resolution is represented in Table 3, where the Fresnel-zone width (Yilmaz, 2001) along the profile is calculated for depths and velocities representing our velocity model. Given that our focus lies mostly within the top 1 km, the maximum Fresnel-zone width does not exceed 270 m, implying features smaller than this are likely still detectable but in the form of diffractions rather than reflections (Malehmir and Bellefleur, 2009). After migration of the data, the lateral resolution is improved (Yilmaz, 2001) to approximately the dominant wavelength. Assuming an average velocity of 5500 m/s, along with the mentioned 35 Hz dominant frequency, the lateral resolution of the migrated section reduces to 157 m.

Table 3. Fresnel-zone width of KBF03A at different depths and velocities.

Depth (km)	Average velocity (km/s)	Fresnel-zone width (m)
2	5.0	380
4	5.5	560
6	6.0	720
8	6.0	830
10	6.0	925
12	6.5	1055
14	6.5	1140

6.2. Seismic attributes

Although the reprocessing steps undertaken in this study have significantly improved the quality of the top 500 ms of the data compared to the original 1994 data, conventional interpretation of the reprocessed data did not allow for the analysis of the data related to the structural features within the Kalahari and Karoo strata to their full potential. Our reprocessed data serve as the basis for generation of composite seismic attributes, which are an innovative way of enhancing the detection of these features in the data. For example, small-scale faulting and folding was recognized on the migrated seismic section with attributes applied, which was not possible with conventional amplitude-based interpretation (Fig. 9). The prominent first-order Moshaweng fault (Tinker et al., 2002) has been imaged and reinterpreted using instantaneous attribute composites. Additionally, the position and orientation of structures (faults) that offset the near-surface strata have been enhanced with a high level of confidence. These features vary in orientation and displacement, as seen in Fig. 9. The Symmetry-Phase

Composite, in particular, has enhanced weak reflections arising from lithological boundaries having minor differences in velocity and density within the Kalahari Group sediments. This is mainly owing to the attribute's insensitivity to the reflection strength of the data (Westgate, 2020). Our results demonstrate that instantaneous attribute composites, with special colour coding, can improve the detection of weak reflections and provide reliable structural interpretations.

6.3. Structural geology

The previous interpretation of the KBF03A and other profiles by Tinker et al. (2002) was focussed primarily on Archaean and Proterozoic tectonic features, with the Moshaweng fault interpreted as one of several crustal-scale Neoarchaean listric normal faults in the Kaapvaal craton. They suggested that the Moshaweng fault was reactivated in a normal sense (NW side downthrown) both before and after Kalahari Group deposition but, apart from suggesting that these events may have been related to two pulses of epeirogenic uplift, respectively following the deposition of the Dwyka and Kalahari groups, they provided no further details.

Our structural interpretation is limited by the 2D nature of the profile, the absence of any surface exposures of the Dwyka Group and the general lack of quality surface outcrop of the Kalahari Group. However, complementary potential-field geophysical data establish the N*E*-SW (040°) orientation of the Moshaweng fault and suggest a broadly N-S trend for the faults inferred at CDP 5100–5160 (Fig. 5). Further information is also offered by lineament analysis of the Kalahari Group along the profile using Google Earth. The satellite imagery reveals a few features in the Kalahari Group with broadly ENE to ESE trends that may provide clues to the orientations of the smaller-scale features mentioned above. We propose here a chronological sequence of tectonic events accounting for the structural features observed in the reprocessed data, with an accompanying illustration shown in Fig. 11.

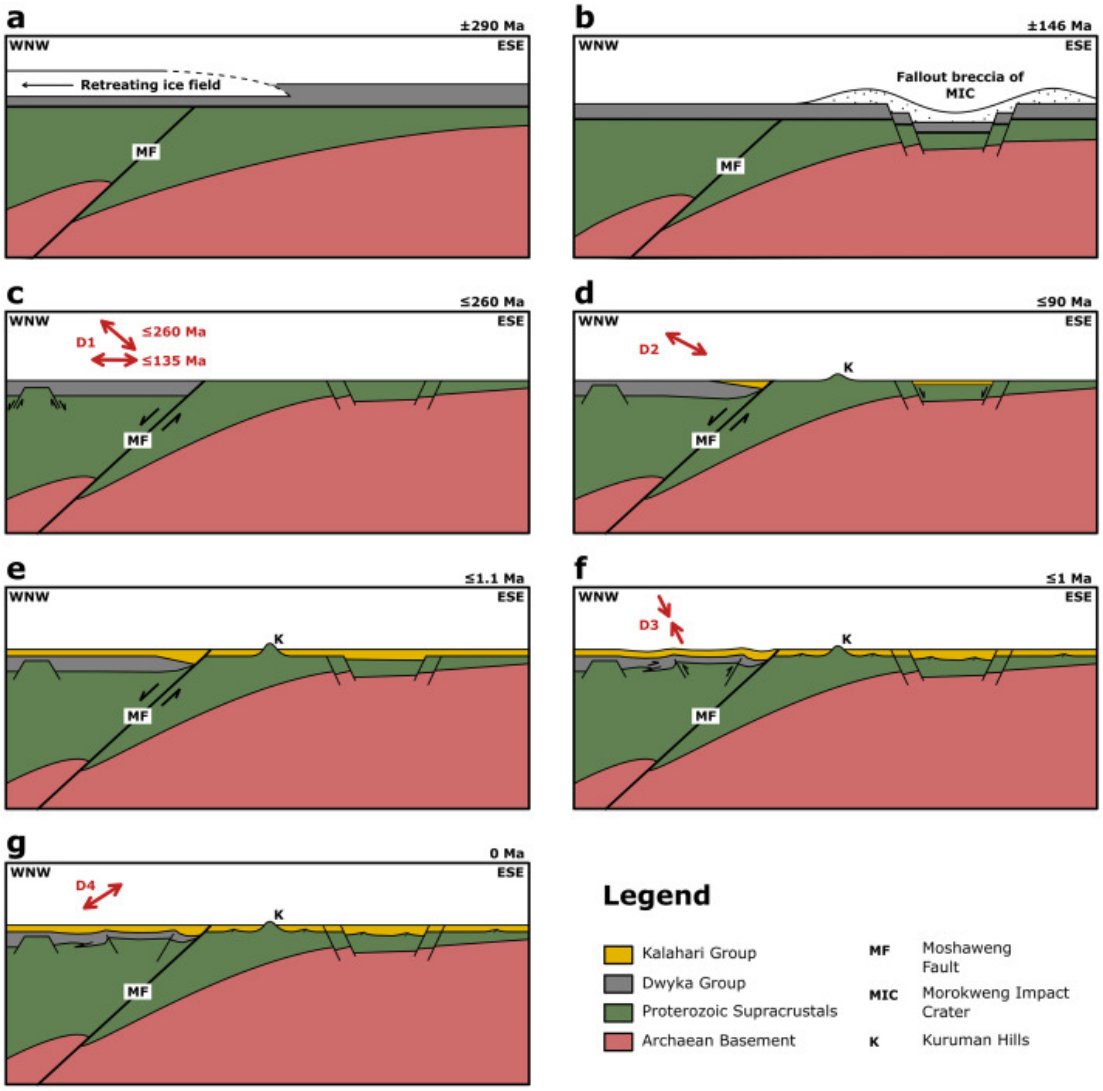

Fig. 11. Schematic proposed tectonic model for the KBF03A seismic profile. Proposed stress events as described in the text are labelled D1 to D4; also shown are features related to the Morokweng impact (b).

6.4. Pre-Kalahari Group structures

As first noted by Du Toit (1933), much of the basement topography of the interior parts of South Africa was largely sculpted by the ~320 to ~290 Ma Dwyka ice sheets, with ±100 m topography north of the KBF03A traverse in Botswana and deep valleys eroded into the Cargonian Highlands to the south of it that are not linked to any obvious basement faults (Visser, 1982; Key and Ayres, 2000). Elsewhere in the Kaapvaal craton, the localised thickening of the Dwyka Group near major, N-S trending Archaean faults is suggestive of their syndepositional extensional reactivation (Visser and Kingsley, 1982). Nevertheless, the lower Karoo Supergroup formations in South Africa display a general absence of significant thickness variations (Visser, 1987; Isbell et al., 2008). Accordingly, Key and Ayres (2000) concluded that *syn*-sedimentary faulting was largely absent in the main Karoo and South Kalahari basins during Dwyka and Ecca deposition. Consequently, given the evidence in the KBF03A profile, we interpret the thinning and termination of the Dwyka Group suboutcrop against the Moshaweng fault as the product of postdepositional tectonics. Estimates of the

amount of post-Dwyka, pre-Kalahari downthrow along the Moshaweng fault depend on whether Dwyka sediments were originally present east of the fault. This has been suggested by Beukes et al. (2019) and may be indicated in the profile by the inclined reflector between the fault and CDP 4000. If the latter does represent the Dwyka unconformity, a minimum estimate of ~100 m is indicated, but if it does not indicate footwall Dwyka Group sediments then throw could have exceeded 200 m. The tomography results inferred from the reflection profile support a sharp drop (~250 m) in the elevation of the pre-Karoo basement west of the Moshaweng fault (Fig. 6).

The second question pertaining to the Moshaweng fault refers to the age of its main reactivation. One solution may be provided by the other, EN*E*- to E-trending faults that affect the Karoo Supergroup rocks in the South Kalahari Basin (Key and Ayres, 2000). The largest of these is the Zoetfontein fault, which coincides with the northern margin of the Kaapvaal craton. It shows downthrow to the NNW that is proposed to be of late Permian age based on regional tectono-stratigraphic and sedimentological considerations (Rust, 1975; Key and Ayres, 2000; Beukes et al., 2019). Whilst a late Permian timing for the NW-side downthrow on the Moshaweng fault and subsequent pre-Kalahari Group erosion can account for the current distribution of the Dwyka Group suboutcrop and the thinning in the immediate hanging wall of the fault, broadly E-W extensional stresses during the Cretaceous related to the opening of the South Atlantic and subsequent continental margin uplift may also have favoured reactivation of the fault in a normal sense before Kalahari Group deposition (Fig. 11).

6.5. Early Kalahari Group extensional structures

Downthrow of the Kalahari Group in the hanging wall of the Moshaweng fault and its associated normal drag folding in both the footwall and hanging wall (Fig. 5) indicate at least one episode of extensional tectonics following development of the Kalahari unconformity and deposition of at least a substantial part of the Kalahari Group. Given the level of disruption caused by the intense faulting in the immediate hanging wall of the Moshaweng fault, it is not possible to determine if the increased thickness of the Kalahari Group between CDP 4180 and CDP 4300 (Fig. 5) reflects original bed thickness variations or subsequent tectonic thickening by folding and/or thrusting. In the first scenario, the localised thickening (by up to 120 m) of the Kalahari Group could be explained by a localised half-graben trough of Wessels Formation conglomerates. While Wessels Formation is absent in the Mamatwan mine ~60 km south of the profile, where Matmon et al. (2015) obtained Pleistocene ages for the Boudin and Eden formations directly overlying the unconformity, the distribution of the Wessels Formation is known to be more highly localised (Haddon and McCarthy, 2005; Gabrielli, 2007). Haddon and McCarthy (2005) noted that the Wessels Formation exhibits sharp facies changes and a gravel-dominated character, and that its clasts are locally derived, poorly sorted and angular; consequently, they interpreted it as the product of stream-reworked debris flow deposits accumulated against active fault scarps. They attributed to it a late Cretaceous age. Based on the above, the Moshaweng fault appears to have experienced at least one further significant post-Dwyka Group extensional episode before the end of the Cretaceous.

6.6. Mid to Late Kalahari Group compressional structures

Evidence of compressional tectonics, in the form of large-scale folds and thrust faults, is ubiquitous across the KBF03A profile, although preferential localisation occurs above and in

the vicinity of pre-existing basement structures, such as the Moshaweng fault and the suspected rim faults related to the Morokweng impact structure (centred on CDPs 2000 and 900; Fig. 5). Our structural interpretation of the Moshaweng fault zone suggests that this event post-dated the main episodes of post-Dwyka extensional faulting. The orientations of the folds and faults cannot be explicitly determined from the 2D profile, but the apparent structural control of the nearby Moshaweng River by WNW-ES*E*-trending lineaments between CDP 800–900, where some of the largest and most intense fold and fault structures are located close to surface, could suggest a broadly E-W strike. A similar E-W-trend for folds with wavelengths of hundreds of metres and associated thrusts is observed in the mid to upper Kalahari Group sediments (Boudin and Eden Formations) at the Kudumane/Hotazel Mine 66 km south of the profile (A. Gregory, personal comm., 2019), where Matmon et al. (2015) obtained cosmogenic burial ages of ~1.1 Ma for the mid- to upper parts of the Kalahari Group stratigraphy near Mamatwan Mine south of Hotazel. In summary, we argue that the fold-and-thrust features in the KBF03A profile not only bear a strong resemblance to the structures in the Kudumane Mine but that they both require a regional, broadly NNE-SSW to NNW-SSE horizontal σ_1 tensor. A NNE-SSW orientation for σ_1 would favour strike-slip to transtensional motion along the NE-SW-trending Moshaweng fault; however, at the scale of resolution of the potential field geophysics there does not appear to have been substantial strike-slip displacement of the Cretaceous age Machavie Dyke (Fig. 2). An orientation of σ_1 closer to NNW-SSE than NNE-SSW, with σ_2 oriented ENE-WSW, would favour largely reverse dip-slip motion on a NE-striking fault. It is not clear that such motion occurred on the main Moshaweng fault; however, reverse movement on faults in the immediate hanging wall explains the prominent fold structure in the Kalahari Group at CDP 4300 (Fig. 5, Fig. 9).

6.7. Tectonic model

The reprocessing of the legacy seismic profile KBF03A shows that Dwyka and Kalahari groups contain direct structural evidence of at least two tectonic events, with a further event constrained by regional evidence, as well as the contemporary stress field: (1) Post-Dwyka, pre-Kalahari normal faulting along the Moshaweng fault and the faults at CDPs 4300–4700 and 5100–5160 (**D1**, 2) Folding and reverse/thrust faulting distributed throughout the profile, and including inversion of at least some parts of the Moshaweng fault zone (**D3**). From regional evidence a further extensional event (**D2**) may also have occurred along the Moshaweng fault associated with the proposed onset of Kalahari Group deposition in the Late Cretaceous. Finally, a **D4** event is included to illustrate the state of the modern stress field. These events are illustrated in Fig. 11 and a proposed timeline of these events is discussed below, with an illustration of the latter events shown in Fig. 12:

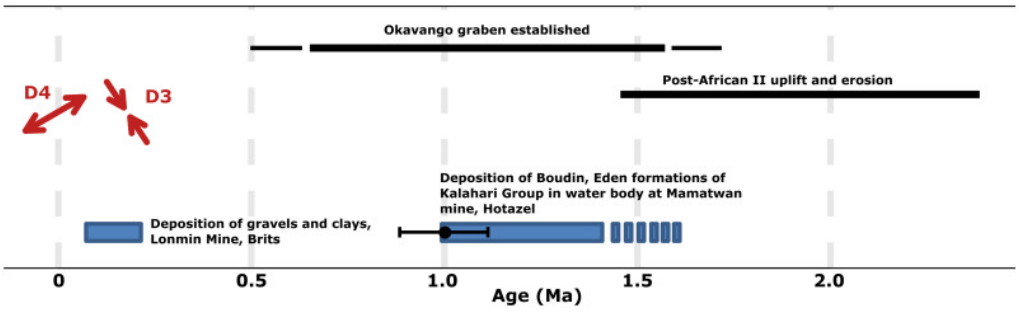

Fig. 12. Timeline of stress events D3 to D6 alongside other major tectonic events. Age of Mamatwan Mine samples of the earliest Kalahari Group deposits are after Matmon et al. (2015).

6.7.1. D1 Event

Based on regional plate-scale stress reconstructions, alternative timings for post-Dwyka, pre-Kalahari Group reactivation of the ancestral Moshaweng fault include: (a) Late Permian N-S to NW-SE extensional tectonics affecting the South Kalahari Basin (Rust, 1975; Key and Ayres, 2000); (b) Early Cretaceous (135–115 Ma) rifting of Africa and South America, during which N-S S_{Hmax}/σ_2 and E-W S_{HMin}/σ_3 extensively reactivated NNE-trending Pan African structures to the west of the study area (Viola et al., 2012); and (c) Mid Cretaceous (115–90 Ma) continental margin uplift that is also observed in off-craton areas to the west of the profile (Viola et al., 2012; Kounov et al., 2009). The faults defining the horst block at CDP 5100–5160 (Fig. 5) would be ideally oriented for dip slip displacements under an E-W S_{Hmin}, N-S S_{Hmax} regime, as illustrated in Fig. 11c. However, the oblique strike of the Moshaweng fault relative to E-W or N-S principal stress directions would have likely generated more complex oblique displacements across the fault. Given the uncertainty around the precise age of the Kalahari Group unconformity and Wessels Formation, it is equally possible that stress conditions related to (c), and possibly even the latter stages of (b), may have been continuous with D2.

6.7.2. D2 event

As previously discussed, no direct evidence of Wessels Formation against the Moshaweng fault has yet been documented; however, it is postulated based on the evidence of localised thickening of the Kalahari Group in the hanging wall of the fault seen in the reprocessed profile (Fig. 5) and regional isopach data (Haddon, 2004; Fig. 3). Reactivation of the fault may correspond to the ±80–65 Ma Campanian - Maastrichtian rifting/extensional event (Fig. 11d) identified further to the east in the Kaapvaal craton where deep NE-SW-trending lithospheric faults facilitated emplacement of the Group I kimberlites, and in NE Africa (Guiraud and Bosworth, 1997; Jelsma et al., 2004; Viola et al., 2012; Tappe et al., 2018). This stress field has been attributed by Jelsma et al. (2009) to changes in motion and/or velocity of the African plate.

6.7.3. D3 Event

The folds and/or thrust faults affecting the beds of the Kalahari Group in the KBF03A profile are not unique to the vicinity of the seismic line. Similar features are observed in the open cast pits of the Kudumane/Hotazel Mine and at several other, widely spaced, localities elsewhere in the western, central and southern parts of the Kaapvaal craton. These include: (1) the open cast pits of the Rockwell Mine near Douglas, ~300 km south of the KBF03A profile, where calcretized Orange River gravels of Miocene-Pliocene age have been folded and thrusted southwards together with their Dwyka Group footwall (Northcote, 2014; T. Marshall, 2017, person. Commun.); (2) SSE-directed thrust faults in calcrete at a quarry near Bultfontein, ~400 km SE of the profile (Andreoli et al., 1996; Tabola et al., 2013; D. Delvaux De Fenffe, unpublished data); and (3) SSE-verging thrust faults in the open cast Sonop Pit of the Lonmin Mine near Brits, ~400 km ENE of the profile (Steenkamp et al., 2018) (Fig. 12).

The cause of this Pleistocene-age, NNW–SSE to N-S, S_{Hmax}/σ_1 with S_{Hmin}/σ_2 oriented ENE-WSW to E-W (Fig. 11f) remains elusive. Numerical models built to model the post-Jurassic to contemporary orientation and character of the stress field in the crust/lithosphere of the African plate in general, and southern Africa in particular, only predict an extensional regime (Coblentz and Sandiford, 1994; Hartnady, 2002; Behn et al., 2004; Bird et al., 2006; Stamps

et al., 2010; Gaina et al., 2013; Tutu et al., 2018; Wang et al., 2020). Although the available evidence indicates that compressional SSE- to S-vergent fault-fold structures developed very recently over a wide area in the Kaapvaal craton, the limited and widely spaced nature of the sites, as well as the strong likelihood that their locations, and possibly also their orientations, are controlled by underlying basement structures (e.g. Viola et al., 2012), warrants caution before interpreting these features in terms of a single craton-wide event.

6.7.4. D4 stress regime

For completeness, it is necessary to summarize the main characteristics of the contemporary neotectonic conditions in the profile area within their southern African context, as extensively reported in the literature (Coblentz and Sandiford, 1994; Andreoli et al., 1996; Bird et al., 2006; Stamps et al., 2010; Tutu et al., 2018; Wang et al., 2020). Among such works, Bird et al. (2006) applied thin shell finite element modelling techniques and produced a set of maps of the patterns of stress and strain of the African crust below latitude 10° S. The model that best fits the available tectonic and geodetic data (focal seismic solutions, borehole breakouts, and rock mechanics indicators) shows that the subcontinent is currently largely in a state of horizontal extension (prone to normal faulting) because its high topographic elevation leads to density moments exceeding those of the spreading ridges flanking the plate. These results are mirrored in recent geodynamic studies of southern Africa from global and plate scale perspectives (Stamps et al., 2010; Tutu et al., 2018; Wang et al., 2020), and thus suggest that the D3 features are not representative of the contemporary regional stress regime (Fig. 11, Fig. 12).

7. Conclusions

Reprocessing the 150 km long legacy seismic profile KBF03A (6 s TWT) has yielded an improved image of the supracrustal Phanerozoic sediment packages found in the vicinity of the western margin of the Kaapvaal craton. In particular, with the incorporation of complex seismic attributes and first-break traveltime tomography, the better imaged 320–290 Ma Dwyka Group and < 90 Ma Late Cretaceous to Cenozoic Kalahari Group sediments reveal polyphasic reactivation of basement structures, under both extensional and compressional stress regimes. Repeated extensional reactivation of a major Neoarchaean-Proterozoic fault (Moshaweng fault) may have occurred in both Permian and Cretaceous times and was followed in Pleistocene times by renewed extension, and later by inversion related to distributed fold-thrust-style deformation. Our analysis provides a new perspective for investigating the Late Mesozoic to Cenozoic tectonics of southern Africa.

Data availability

Seismic research data are not shared. Geological outcrop and magnetic map data can be found on the website of The Council for Geoscience South Africa (http://www.geoscience.org.za/index.php/2019-03-13-12-40-41).

Declaration of Competing Interest

The authors declare that they have no known competing financial interests or personal relationships that could have appeared to influence the work reported in this paper.

Acknowledgments

The donation of seismic data by AngloGold Ashanti, Ltd., is gratefully acknowledged. The Council for Geoscience is also thanked for providing outcrop and magnetic data. The work presented here was facilitated by the Seismic Research Centre at the University of the Witwatersrand. The support of the DSI-NRF Centre of Excellence (CoE) for Integrated Mineral and Energy Resource Analysis (DSI-NRF CIMERA) towards this research is hereby acknowledged. Opinions expressed and conclusions arrived at are those of the authors and are not necessarily to be attributed to the CoE. Finally, the authors would like to thank the editor and reviewers for their valued feedback.

References

Adam, E., Milkereit, B., Mareschal, M., 1998. Seismic reflection and borehole geophysical investigations in the Matagami mining camp. Can. J. Earth Sci. 35, 686–695.

Alebouyeh Semami, F., de Kock, M.O., S¨oderlund, U., Gumsley, A., da Silva, R., Beukes, N.J., Armstrong, R., 2016. New U–Pb geochronologic and palaeomagnetic constraints on the late Palaeoproterozoic Hartley magmatic event: evidence for a potential large igneous province in the Kaapvaal Craton during Kalahari assembly, South Africa. GFF 138 (1), 164–182.

Andreoli, M.A.G., Doucour´e, M., Van Bever Donker, J., Brandt, D., Andersen, N.J.B., 1996. Neotectonics of Southern Africa - a review. Africa Geosci. Rev. 3, 1–16.

Bangert, B., Stollhofen, H., Lorenz, V., Armstrong, R., 1999. The geochronology and significance of ash-fall tuffs in the glaciogenic Carboniferous-Permian Dwyka Group of Namibia and South Africa. J. Afr. Earth Sci. 29, 33–49.

Barnes, A.E., 2000. Weighted average seismic attributes. Geophysics 65 (1), 275–285.

Bateman, M.D., Thomas, D.S., Singhvi, A.K., 2003. Extending the aridity record of the Southwest Kalahari: current problems and future perspectives. Quat. Int. 111, 37–49.

Behn, M.D., Conrad, C.P., Silver, P.G., 2004. Detection of upper mantle flow associated with the African Superplume. Earth Planet. Sci. Lett. 224, 259–274.

Beukes, N.J., de Kock, M.O., Vorster, V., Ravhura, L.G., Frei, D., Gumsley, A.P., Harris, C., 2019. The age and country rock provenance of the Molopo Farms complex: implications for Transvaal Supergroup correlation in southern Africa. S. Afr. J. Geol. 122 (1), 39–56.

Bird, P., Ben-Avraham, Z., Schubert, G., Andreoli, M., Viola, G., 2006. Patterns of stress and strain rate in southern Africa. J. Geophys. Res. 111, B08402.

Brown, A.R., 1996. Seismic attributes and their classification. Lead. Edge 15 (10), 1090–1195.

Catuneanu, O., 2004. Basement control on flexural profiles and the distribution of foreland facies: the Dwyka Group of the Karoo Basin, South Africa. Geology 32 (6), 517–520.

Catuneanu, O., Wopfner, H., Eriksson, P.G., Cairncross, B., Rubidge, B.S., Smith, R.M.H., Hancox, P.J., 2005. The Karoo basins of south-Central Africa. J. Afr. Earth Sci. 43 (1–3), 211–253.

Coblentz, D.D., Sandiford, M., 1994. Tectonic stresses in the African plate: constraints on the ambient lithospheric stress state. Geology 22, 831–834.

Corner, B., Reimold, W.U., Brandt, D., Koeberl, C., 1997. Morokweng impact structure, Northwest Province, South Africa: geophysical imaging and shock petrographic studies. Earth Planet. Sci. Lett. 146 (1–2), 351–364.

Du Toit, A.L., 1933. Crustal movement as a factor in the geographical evolution of southern Africa. S. Afr. Geogr. J. 16, 3–20.

Gabrielli, F., 2007. 2622 Morokweng Sheet 1:250,000 Scale. South African Council for Geoscience, Pretoria.

Gaina, C., Torsvik, T.H., van Hinsbergen, D.J.J., Medvedev, S., Werner, S.C., Labails, C., 2013. The African Plate: a history of oceanic crust accretion and subduction since the Jurassic. Tectonophysics 604, 4–25.

Guiraud, R., Bosworth, W., 1997. Phanerozoic geodynamic evolution of northeastern Africa and the northwestern Arabian platform. Tectonophysics 315, 73–108.

Haddon, I.G., 2004. The sub-Kalahari Geology and Tectonic Evolution of the Kalahari basin, Southern Africa. University of the Witwatersrand, Johannesburg, p. 343 (PhD thesis).

Haddon, I.G., McCarthy, T.S., 2005. The Mesozoic – Cenozoic interior sag basins of Central Africa: the Late-cretaceous – Cenozoic Kalahari and Okavango basins. J. Afr. Earth Sci. 43, 316–333.

Hart, R.J., Andreoli, M.A.G., Tredoux, M., Moser, D., Ashwal, L.D., Eide, E.A., Webb, S.J., Brandt, D., 1997. Late Jurassic age for the Morokweng impact structure, southern Africa. Earth Planet. Sci. Lett. 147, 25–35.

Hartnady, C.J.H., 2002. Earthquake hazard in Africa: perspectives on the Nubia-Somalia boundary. S. Afr. J. Sci. 98, 425–428.

Henkel, H., Reimold, W.U., Koeberl, C., 2002. Magnetic and gravity model of the Morokweng impact structure. J. Appl. Geophys. 49, 129–147.

Iacopini, D., Butler, R.W.H., Purves, S., McArdle, N., De Freslon, N., 2016. Exploring the seismic expression of fault zones in 3D seismic volumes. J. Struct. Geol. 89, 54–73.

Isbell, J.L., Cole, D.I., Catuneanu, O., 2008. Carboniferous-Permian glaciation in the main Karoo Basin, South Africa: stratigraphy, depositional controls, and glacial dynamics. Geol. Soc. Am. 441, 71–82.

Jelsma, H., Barnett, W., Richards, S., Lister, G., 2009. Tectonic setting of kimberlites. Lithos 112 (1), 155–165.

Jelsma, H.A., De Wit, M., Thiart, C., Dirks, P.H.G.M., Viola, G., Basson, I.J., Anckar, E., 2004. Preferential distribution along transcontinental corridors of kimberlites and related rocks of Southern Africa. S. Afr. J. Geol. 107, 301–324.

Kenkmann, T., Poelchau, M.H., Wulf, G., 2014. Structural geology of impact craters. J. Struct. Geol. 62, 156–182.

Kenny, G.G., Harrigan, C.O., Schmitz, M.D., Crowley, J.L., Wall, C.J., Andreoli, M.A.G., Gibson, R.L., Maier, W.D., 2021. Timescales of impact melt sheet crystallization and the precise age of the Morokweng impact structure, South Africa. Earth Planet. Sci. Lett. [submitted for publication].

Key, R.M., Ayres, N., 2000. The 1998 edition of the National Geological Map of Botswana. J. Afr. Earth Sci. 30 (3), 427–451.

Kim, J., Moon, W.M., Percival, J.A., Gordon West, F., 1992. Seismic imaging of shallow reflectors in the eastern Kapuskasing structural zone, with corrections of crossdip attitudes. Geophys. Res. Lett. 19 (20), 2035–2038.

Koeberl, C., Armstrong, R.A., Reimold, W.U., 1997. Morokweng, South Africa: a large impact structure of Jurassic-cretaceous boundary age. Geology 25, 731–734.

Kounov, A., Viola, G., de Wit, M., Andreoli, M.A.G., 2009. Denudation along the Atlantic passive margin: new insights from apatite fission-track analysis on the western coast of South Africa. Geol. Soc. Lond., Spec. Publ. 324, 287–306.

Lithgow-Bertelloni, C., Silver, P.G., 1998. Dynamic topography, plate driving forces and the African superswell. Nature 395, 269–272.

Malajczuk, S., Saklani, R., Clark, D., Eastwell, D., 2016. Improved subsurface imaging and interpretability through broadband reprocessing of legacy seismic data examples from North West Shelf Australia. In: 25th ASEG-PESA-AIG Geophysical Conference and Exhibition, pp. 1–8.

Malehmir, A., Bellefleur, G., 2009. 3D seismic reflection imaging of volcanic-hosted massive sulphide deposits: Insights from re-processing Halfmile Lake data, New Brunswick, Canada. Geophysics 74, B209–B219.

Malehmir, A., Donoso, G., Markovic, M., Maries, G., Dynesius, L., Brodic, B., Pecheco, N., Marsden, P., B¨ackstr¨om, E. Penney, Araujo, V., 2019. Smart Exploration: from legacy data to state-of-the-art data acquisition and imaging. First Break 37 (8), 71–74.

Manzi, M., Malehmir, A., Durrheim, R., 2018. Improved subsurface imaging through re-processing of Legacy 2D Seismic Data-A case study from a Deep South African Gold Mine. In: EAGE 2nd Conference on Geophysics for Mineral Exploration and Mining.

Manzi, M., Malehmir, A., Durrheim, R., 2019. Giving the legacy siemsic data the attention they deserve. First Break 37 (8), 89–96.

Matmon, A., Hidya, A.J., Vainer, S., Crouvi, O., Fink, D., Erel, Y., 2015. New chronology for the southern Kalahari Group sediments with implications for sediment-cycle dynamics and early hominin occupation. Quat. Res. 84 (1), 118–132.

Nedimoví c, M.R., West, G.F., 2003. Crooked-line 2D seismic reflection imaging in crystalline terrains. Geophysics 68 (1), 16–409.

Northcote, C.L., 2014. Neo-Tectonics in the Dwyka Tillite and the Tertiary Diamondiferous Gravels of the Mid Orange River, South Africa. B. Sc. Hons. Project. University of Pretoria, South Africa, p. 30.

Nyblade, A.A., Robinson, S.W., 1994. The African Superswell. Geophys. Res. Lett. 21 (9), 765–768.

Opdyke, N.D., Mushayandebvu, M., de Witt, M.J., 2001. A new palæomagnetic pole for the Dwyka System and correlative sediments in sub-Saharan Africa. J. Afr. Earth Sci. 33 (1), 143–153.

Partridge, T.C., Maud, R.R., 1987. Geomorphic evolution of southern Africa since the Mesozoic. S. Afr. J. Geol. 90 (2), 179–208.

Partridge, T.C., Botha, G.A., Haddon, I.G., 2006. Cenozoic deposits of the interior. In: Johnson, M.R., Anhaeusser, C.R., Thomas, R.J. (Eds.), The Geology of South Africa, 585–604. Geological Society of South Africa.

Pretorius, C.C., Muller, M.R., Larroque, M., Wilkins, C., 2003. A review of 16 years of hardrock seismics on the Kaapvaal craton, Hardrock Seismic Exploration. In: Eaton, D., Salisbury, M., Milkereit, B. (Eds.), Developments in Geophysics Series, 2003. SEG, Houston, pp. 247–268.

Reimold, W.U., Armstrong, R.A., Koeberl, C., 2002. A deep drillcore from the Morokweng impact structure, South Africa: petrography, geochemistry, and constraints on the crater size. Earth Planet. Sci. Lett. 201, 221–232.

Rust, I.C., 1975. The sedimentary and tectonic framework of Gondwana basins in Southern Africa in Gondwana Geology. In: Campbell, K.S.W. (Ed.), Papers from the third Gondwana Symposium, Canberra, Australia. A.N.U Press, pp. 537–564.

Scheiber-Enslin, S.E., Manzi, M.S.D., 2018. Integration of 3D reflections seismics and magnetic data for deep platinum mine planning and risk mitigation: a case study from the Bushveld complex, South Africa. Explor. Geophys. 49 (6), 928–939.

Smit, P.J., 1974. Geological Map, Sheet 2622 Morokweng, Scale 1:250,000, Council for Geoscience, Pretoria (1974) One Sheet.

Stamps, D.S., Flesch, L.M., Calais, E., 2010. Lithospheric buoyancy forces in Africa from a thin sheet approach. Int. J. Earth Sci. 99, 1525–1533.

Steenkamp, J.M.A., van der Westhuizen, W.A., Bateman, M.D., Jacobson, L., Nel, L., 2018. A Pleistocene thrust fault in anorthosite of the Rustenburg Layered Suite near Mooinooi, North West province, South Africa: neotectonic implications. S. Afr. J. Geol. 121 (4), 421–430.

Tabola, K.P., Andreoli, M.A.G., Bumby, A., Delvaux-de Fenffe, D., 2013. Neotectonic fault mapping in calcrete at Bultfontein, Free State, South Africa. Necsa (Open File) document NLM-REP-14/048, p. 39.

Taner, M.T., Koehler, F., Sheriff, R.E., 1979. Complex seismic trace analysis. Geophysics 44 (6), 1041–1063.

Tankard, A., Welsink, H., Aukes, P., Newton, R., Stettler, E., 2012. 23 – Geodynamic interpretation of the Cape and Karoo basins, South Africa. In: Roberts, D.G., Bally, A. W. (Eds.), Regional Geology and Tectonics: Phanerozoic Passive Margins, Cratonic Basins and Global Tectonic Maps. Elsevier, pp. 868–945.

Tappe, S., Smart, K., Torsvik, T., Massuyeau, M., de Wit, M., 2018. Geodynamics of kimberlites on a cooling Earth: clues to plate tectonics evolution and deep volatiles cycles. Earth Planet. Sci. Lett. 484, 1–14.

Thomas, D.D., O'Connor, P., Bateman, M.D., Shaw, P., Stokes, S., Nash, D., 2000. Dune activity as a record of late Quaternary aridity in the northern Kalahari: new evidence from northern Namibia interpreted in the context of regional arid and humid chronologies. Palaeogeogr. Palaeoclimatol. Palaeoecol. 156, 107–134.

Tinker, J., de Wit, M., Grotzinger, J., 2002. Seismic stratigraphic constraints on Neoarchean – Paleoproterozoic evolution of the western margin of the Kaapvaal craton, South Africa. S. Afr. J. Geol. 105, 107–134.

Tutu, A.O., Steinberger, B., Sobolev, S.V., Rogozhina, I., Popov, A.A., 2018. Effects of upper mantle heterogeneities on the lithospheric stress field and dynamic topography. Solid Earth 9, 649–668.

Vainer, S., Dor, Y.B., Matmon, A., 2018a. Coupling cosmogenic nuclides and luminescence dating into a unified accumulation model of aeolian landforms age and dynamics: the case study of the Kalahari Erg. Quat. Geochronol. 48, 133–144.

Vainer, S., Erel, Y., Matmon, A., 2018b. Provenance and depositional environments of Quaternary sediments in the southern Kalahari Basin. Chem. Geol. 476, 352–369.

Van Niekerk, H.S., Beukes, N.J., 2019. Revised definition/outline of the Kheis Terrane along the western margin of the Kaapvaal Craton and lithostratigraphy of the newly proposed Keis Supergroup. S. Afr. J. Geol. 122 (2), 187–220.

Viola, G., Kounov, A., Andreoli, M.A.G., Mattila, J., 2012. Brittle tectonic evolution of the basement granites in the Vaalputs area: more than 500 my of continued reactivation. Tectonophysics 514-517, 93–114.

Visser, J.N.J., 1982. An analysis of the Permo-Carboniferous glaciation in the Marine Kalahari basin, southern Africa. Palaeogeogr. Palaeoclimatol. Palaeoecol. 44, 295–315.

Visser, J.N.J., 1987. The palaeogeography of part of southwestern Gondwana during the Permo-Carboniferous glaciation. Palaeogeogr. Palaeoclimatol. Palaeoecol. 61, 205–219.

Visser, J.N.J., Kingsley, C.S., 1982. Upper Carboniferous glacial valley sedimentation in the Karoo Basin, Orange Free State. Geol. Soc. S. Afr. Trans. 85, 71–79.

Wang, X., Holt, W.E., Ghosh, A., 2020. Data for "joint modeling of lithosphere and mantle dynamics: sensitivity to viscosities within the lithosphere, asthenosphere, transition zone, and D" layers. Data Brief 2, 104935.

Wela, S.S., 2017. A lithological, petrographic and geochemical investigation of the M4 borehole core, Morokweng Impact Structure, South Africa. MSc Dissertation. University of the, Witwatersrand, Johannesburg.

Westgate, M., 2020. Reappraisal of Legacy Reflection Seismic Data using Advanced Processing Techniques and Seismic Attributes. PhD Thesis. University of the Witwatersrand, South Africa.

White, R.E., 1991. Properties of instantaneous attributes. Lead. Edge 10 (7), 1–68.

Widess, M.B., 1973. How thin is a thin bed? Geophysics 38 (6), 1176–1180.

Woodward, M.J., 1992. Wave-equation tomography. Geophysics 57 (1), 15–26.

Yilmaz, O., 2001. Seismic data analysis: processing, inversion and interpretation of seismic data. Soc. Explor. Geophys. https://doi.org/10.1190/1.9781560801580.1803-1807.